Radiogenic Isotopes Document the Start of Subduction in the Western Pacific

Hong-Yan Li[a], Rex N. Taylor[b], Julie Prytulak[c1] , Maria Kirchenbaur[d2], John Shervais[e], Jeffrey G. Ryan[f], Marguerite Godard[g], Mark K. Reagan[h], Julian A. Pearce[i3]

[a]State Key Laboratory of Isotope Geochemistry, Guangzhou Institute of Geochemistry, Chinese Academy of Sciences, Guangzhou 510640, P.R. China

[b]School of Ocean and Earth Science, University of Southampton, NOC, Southampton, SO14 3ZH, UK

[c]Department of Earth Science and Engineering, Imperial College London, London SW7 2AZ, UK

[d]Institut für Mineralogie, Universität zu Köln, Germany

[e]Department of Geology, Utah State University, Logan, UT, USA

[f]School of Geosciences, University of South Florida, Tampa, Florida, USA

[g]Géosciences Montpellier, CNRS, Université de Montpellier, Montpellier, France

[h]Department of Earth and Environmental Sciences, University of Iowa, Iowa City, IA, USA

[i]School of Earth and Ocean Sciences, Cardiff University, Cardiff CF10 3AT, UK

*Corresponding author (pearceja@cf.ac.uk)

[1] Department of Earth Sciences, University of Durham, Durham DH1 3LE

[2] Institut für Mineralogie, Universität zu Köln, Germany

[3] Corresponding author at: School of Earth and Ocean Sciences, Cardiff University, Cardiff CF10 3AT, UK

ABSTRACT

Subduction initiation is one of the least understood aspects of plate tectonics. In an effort to obtain the first *in situ* magmatic record of subduction initiation, the International Ocean Discovery Program Expedition 352 drilled at four sites in the inner trench wall of the Bonin Trench to recover 1.22km of oceanic upper crust accreted within a few m.y. of subduction initiation. The two sites nearer to the trench (U1440 and U1441) yielded axial and off-axis fore-arc basalts (FAB), while those c. 15km further from the trench (U1439 and U1442) yielded axial low-silica boninites and high-Mg andesites overlain by off-axis high-silica boninites. This study uses Hf-Nd-Sr-Pb isotope analysis from c. 50 stratigraphically representative core samples to trace the evolution of the mantle source during the brief period of FAB-through-boninite magmatism immediately following subduction initiation. Results show that: 1) the FAB have high εHf relative to εNd and were derived from variably depleted mantle of 'Indian' provenance with no detectable subduction input; 2) the axial boninites follow mixing trends between a residual FAB mantle source and a subduction component derived from shallow (amphibolite facies) melting of oceanic crust of 'Pacific' provenance; and 3) the off-axis boninites define mixing trends between a hybrid mantle wedge (residual mantle + slab melt) and an additional subduction component with lower εNd and higher $^{207}Pb/^{204}Pb$ that requires a significant contribution from pelagic sediment. This incoming of pelagic sediments may signify a change from an accretionary to non-accretionary margin as

subduction evolves. The results thus indicate a rapidly evolving system in terms of geodynamics, magma genesis and crustal accretion immediately following subduction initiation.

Keywords: Radiogenic isotopes, Subduction initiation, Forearc basalts, Boninites, International Ocean Discovery Program (IODP) Expedition 352.

---

1. Introduction

Unlike most types of plate tectonic process, regional-scale subduction initiation is not taking place at the present-day. In consequence, subduction initiation is one of the least understood aspects of plate tectonics. Much of our limited geological knowledge to date derives from the Izu-Bonin-Mariana (IBM) outer forearc, which carries a full record of magmatic and tectonic activity from the start of subduction in the Eocene to the start of normal arc volcanism some 10 m.y. later (e.g. Ishizuka et al., 2011). It also hosts the type localities for the two rock types characteristic of subduction initiation and fore-arc terranes: forearc basalts (FAB), which are MORB-like tholeiitic basalts (Reagan et al., 2010), and boninites, which are distinctive high-Si, high-Mg, low-Ti volcanic rocks (e.g. Crawford, 1989).

The presence, and close association in space and time, of FAB and boninites during the birth of the IBM system have provided key supporting evidence for geodynamic models of

61 subduction initiation. Notably, the presence of FAB supports the original Stern and Bloomer
62 (1992) hypothesis that subduction initiation was immediately succeeded by subsidence and
63 roll-back of the embryonic subducted slab resulting in an episode of near-trench extension or
64 sea-floor spreading. In addition, the presence of boninites supports the need, in such a model,
65 for a period of anomalous magmatism between initial subsidence and rollback and the
66 establishment of the stable down-dip subduction required for normal island arc volcanism.
67 The type of model proposed by Stern and Bloomer has since been supported by both
68 ophiolite studies (e.g. Shervais, 2001; Dilek and Flower, 2003) and numerical experiments
69 (e.g. Leng et al., 2012).
70
71 Despite much support for this general model, there is, however, much debate over the detail.
72 For the starting conditions, Stern and Bloomer (1992) base their model on the reconstruction
73 of Hussong and Uyeda (1981) and others in which subduction initiation began at a pure
74 strike-slip, transform plate boundary, a setting that continues to be supported by tectonic
75 reconstructions (e.g. Wu et al., 2016). However, Casey and Dewey (1994) argue for a
76 transtensional boundary (a 'leaky' transform fault), which, if correct, may have led to
77 episodes of ridge subduction following subduction initiation. Loci not involving a transform
78 fault have also been proposed. These include a thermal anomaly in the mantle (Macpherson
79 and Hall, 2001), the edge of an oceanic plateau (Niu et al., 2003) and a Mesozoic continental
80 margin (Ishizuka et al. 2018).
81
82 Moreover, although the concept of slab roll-back as the cause of spreading, and hence the

mechanism for FAB genesis, is supported by numerical models, it still requires ground-truthing. To do this, and to constrain better the pre-subduction tectonic setting, one of the optimal approaches is to establish the extent, stratigraphy and genesis of the volcanic rocks erupted immediately following subduction initiation. Because much of this evidence is sediment-covered, drilling is needed. Thus, in 2014, IODP Expedition 352 to the Bonin forearc had the objective of documenting the changing nature and composition of the crust formed immediately after subduction initiation (Reagan et al., 2015). Here, we present the first radiogenic isotope (Hf-Nd-Sr-Pb) data from the Expedition, and use these data to 1) establish the evolution of mantle sources and slab fluxes following subduction initiation and 2) use the resulting information to test, and develop new, hypotheses for the plate configurations and driving forces involved.

2. Materials

IODP Expedition 352 drilled at four sediment-covered sites between the ophiolitic sequence exposed in the inner trench wall in the east and the Bonin Ridge embryonic volcanic arc in the west (Fig. 1 a-b). These subdivide into two deeper, more trench-proximal sites (U1440 and U1441: the 'FAB sites') and two shallower, trench-distal sites (U1439 and U1442: the 'boninite sites'). Representative basement samples taken on-board the drilling ship from each of the petrologic units defined and described at these four sites (Reagan et al., 2015) form the basis for this isotope study.

105 Fig. 1c summarizes the stratigraphies for the holes with the deepest penetration, namely
106 U1440B, U1441A, U1439C, and U1442A. All four recovered lavas, but one of the FAB
107 holes (U1440B) and one of the boninite holes (U1439C) also rooted in sheeted intrusions
108 (Reagan et al., 2015). The probable explanation is that upper oceanic crust was penetrated at
109 both FAB and boninite sites, the former representing crust in the more trench-proximal
110 location. Lava sequences at FAB Site U1440 and boninite Sites U1439 and U1442 have been
111 divided into lower and upper units, each with a number of sub-units. In both FAB and
112 boninite sites, the lower units compositionally match the underlying dikes and henceforth will
113 be termed 'axial', while the upper units are compositionally distinct and will be termed 'off-
114 axis'.
115
116 According to bulk rock Ar-Ar, and CA-TIMS zircon U-Pb, dating (Reagan et al., 2019), the
117 FAB and boninites in this paper formed from an intermediate-rate, sea-floor spreading event
118 that took place between approximately 52 and 50Ma immediately following subduction
119 initiation (Fig. 1c). The Bonin Ridge boninites and their differentiates subsequently erupted
120 onto this oceanic crust between about 50 and 44 Ma to form an embryonic arc, followed by
121 normal tholeiitic and calc-alkaline arc magmatism (e.g. Cosca et al., 1998, Ishizuka et al.,
122 2011).
123
124 In terms of rock type, the FAB are tholeiites and resemble MORB in all but setting and the
125 greater degree of depletion of their mantle source. Shervais et al. (2019) subdivide axial- and
126 off-axis FAB into a main, 'normal' group entitled N-FAB, less common depleted and

enriched groups respectively entitled D-FAB and E-FAB, as well as primitive variants of these not distinguished here. The axial boninites are predominantly made up of low-Si boninites accompanied by their fractionation products, high-Mg andesites (HMA), while off-axis boninites are primarily made up of high-Si boninites (Reagan et al., 2015, 2017).

The preliminary model of Reagan et al. (2017) produces the FAB by decompression melting with little to no slab flux. Melting of an extremely depleted (harzburgitic) mantle flushed with fluids and/or melts from subducted sediments and oceanic crust then generated boninites. Shervais et al. (2019) refine the petrogenesis of the FAB, providing evidence that their mantle source had higher potential temperatures than normal MORB but was more depleted due to an episode of prior, garnet-facies depletion.

3. Methods

Table 1 provides a subset of the data used in the geochemical plots, and the text below provides a brief summary of analytical methods and quality controls. Appendix A contains sample locations and the full element and isotope data, set and Appendix B gives full analytical detail.

3.1 Preparation procedure

Following crushing and agate milling, we analysed these samples for major elements by XRF

149 at Utah State University and trace elements by ICP-MS at Guizhou Tongwei Analytical
150 Technology Co. Ltd. (Appendix B, Section 2). We heavily leached altered samples for
151 analysis of isotopes of the alteration-mobile elements Sr and Pb (see Appendix B, Sections
152 3.3 and 5 for leaching procedures), but some analyses retained evidence of metasomatism,
153 with Pb isotopes in FAB particularly affected. In such cases, if there was fresh glass or rock
154 nearby, we reanalysed Pb isotopes using the fresh material.
155
156 *3.2 Analytical methods*.
157
158 We analysed Hf isotope ratios at the Guangzhou Institute of Geochemistry, Chinese
159 Academy of Sciences (GIGCAS) on a Neptune MC-ICPMS (Appendix B, Section 3). We
160 took particular care to check for complete sample dissolution and hence avoid the potential
161 problem of small, residual zircons (Appendix B: Section 7 and Table B.5). We report the Hf
162 isotopic ratios relative to a $^{176}Hf/^{177}Hf$ ratio of 0.282189 for JMC14374 (corresponding to a
163 value for JMC475 of 0.282158).
164
165 We also carried out neodymium isotope ratio analyses at GIGCAS on the Neptune MC-
166 ICPMS (Appendix B, Section 3). We report the Nd isotopic ratios relative to $^{143}Nd/^{144}Nd$ of
167 JNdi-1=0.512115. We carried out further Nd isotope analyses in the MAGIC laboratories at
168 Imperial College London with a Nu Instruments HR MC-ICPMS, also using neodymium
169 standard, JNdi. (Appendix B, Section 4). Analyses of USGS reference materials, BCR-2,
170 BIR1a and BHVO-2, run as unknowns demonstrate excellent agreement both between the

two laboratories and with accepted values (Appendix B, Table B.3). We determined Sr isotope ratios at both GIGCAS and the MAGIC using a Thermo Finnigan Triton thermal ionization mass spectrometer (TIMS) (Appendix B, Sections 3 and 4). Both laboratories report the Sr isotopic ratios relative to $^{87}Sr/^{86}Sr$ of NBS-987 = 0.710248. Appendix B, Table B.2 gives international standard data obtained by the two laboratories.

We measured Pb isotope ratios on a Thermo Neptune MC-ICP-MS at the University of Southampton UK, using a double spike to correct for instrumental mass fractionation (Appendix B, Section 5). Procedural blanks range between 30-95 pg Pb. NBS SRM 981 values achieved during the measurement period were $^{206}Pb/^{204}Pb$=16.9404±32,$^{207}Pb/^{204}Pb$ = 15.4969±32, $^{208}Pb/^{204}Pb$ = 36.7149±90 (2s.d.; n=44). Propagated uncertainties for combined natural sample and spiked sample analyses were always less than the reproducibility 2σ of NBS SRM 981.

Several diagrams in this paper combine our data with published data from other laboratories. Only Nd isotopes exhibited significant inter-laboratory variation. All data used in this paper have thus been normalized to $^{143}Nd/^{144}Nd$ of 0.511858 for the La Jolla standard, which is equivalent to the JNdi value of 0.512115. We provide checks for internal consistency of these various data sets in Appendix B, Section 6. In the text that follows, we describe and explain the principal isotopic features under 'Results' and the more detailed isotopic component modeling under 'Interpretations'.

193 # 4. Results

194

195 *4.1 Isotope stratigraphy*

196

197 Fig. 2 gives the isotope stratigraphies for the four principal Exp. 352 holes. Off-axis FAB
198 from U1440B have distinctively high εHf_i, low εNd_i and high $^{206}Pb/^{204}Pb$. The axial-FAB
199 (both lavas and dikes) are predominantly homogenous N-FAB compositions. Exceptions are
200 the single analysed sample of E-FAB, which has distinctly lower εNd_i and slightly lower
201 εHf_i, and the single analysed sample of D-FAB, which has distinctly higher εNd_i and slightly
202 higher εHf_i. There is no significant difference between the axial N-FAB compositions from
203 the two FAB holes.

204

205 Off-axis boninites have lower εNd_i and lower or similar εHf_i compared to axial-boninites, but
206 higher or similar Sr and Pb isotope ratios. The axial-boninites are more variable than the
207 axial-FAB, likely reflecting their more complex genesis, which includes magma mingling
208 (Reagan et al., 2015). There is no significant compositional difference between the off-axis
209 boninites from the two holes, but there are small differences between axial-boninites (e.g.
210 lower average $^{206}Pb/^{204}Pb$ and higher average εNd_i in Hole U1442A). Compared to the FAB,
211 all boninites have lower εHf_i and higher $^{206}Pb/^{204}Pb$.

212

213 *4.2 Principal Hf, Nd, Sr and Pb element characteristics*

214

215 Figure 3 depicts chondrite-normalized REE patterns extended to include Pb, Sr and Hf in
216 positions that maintain the order of incompatibility during melting of the upper mantle.
217 Appendix A provides the full data set used for these patterns and for the means and standard
218 deviations reported below. It also provides values for other petrogenetically significant trace
219 elements,
220
221 For the FAB sites, mantle sources were variably depleted, as reflected in the variable slopes
222 of the REE patterns in Fig. 3a. Of the axial-FAB, the E-FAB sample has the least LREE-
223 depletion (Ce/Yb=2.46) and D-FAB (Ce/Yb=0.96) the greatest. The axial N-FAB have
224 intermediate levels of depletion (Ce/Yb=1.50±0.13[1σ]) as do off-axis N-FAB
225 (Ce/Yb=1.63±0.05[1σ]). However, all the FAB are significantly more depleted than average
226 N-MORB (Ce/Yb=3.8±0.2[1σ] and D-MORB ((Ce/Yb=3.0±0.2[1σ]) (data of Gale et al.,
227 2013). Strontium and Pb show no selective element enrichments that might indicate a
228 subduction component, provided the patterns are restricted to glass and the least-altered
229 rocks.
230
231 For the boninite sites (Fig. 3b-c), all samples are significantly enriched in Sr and Pb relative
232 to the surrounding REE, a characteristic of all arc-related lavas. Unlike most arc lavas,
233 however, they exhibit pronounced positive Hf anomalies, features commonly associated with
234 subduction initiation (e.g. Hickey-Vargas, 1989; Pearce et al., 1999). Their low
235 concentrations of the subduction-immobile HREE indicate very depleted mantle sources,
236 significantly more depleted than FAB sources. Their LREE enrichments

237 Ce/Yb=3.05±0.44[1σ]) are, however, greater than most FAB, so requiring modification of
238 this depleted mantle by a LREE-enriched subduction component. Thus Nd must have been
239 subduction-mobile during boninite genesis. Relative to Sr, Pb and Hf, however, chondrite-
240 normalized Nd concentrations are low, and hence the mobility of Nd during subduction must
241 also have been comparatively low.
242
243 The difference between axial-boninites (Fig. 3b) and off-axis boninites (Fig. 3c) is less
244 obvious than that between FAB and boninites. Primarily, the off-axis boninites have the
245 larger Pb, Sr and Hf peaks, lower and variable concentrations of the HREE for a given MgO
246 content, and slight LREE enrichment (Ce/Yb=3.82±1.23[1σ]) rather than depletion. These
247 features indicate that the off-axis boninites likely experienced greater degree of mantle
248 depletion and a greater contribution from a subduction component containing all daughter
249 elements (Pb, Sr, Hf and Nd).
250
251 *4.3 Principal Sr, Nd, Hf, Pb isotope ratio covariations*
252
253 Fig. 4 summarizes the radiogenic isotope evolution from 1) axial-FAB to off-axis FAB which
254 defines the ambient mantle before subduction and then 2) from FAB to axial-boninite which
255 defines the first stage of subduction and finally 3) from axial-boninite to off-axis boninite
256 which defines the beginning of embryonic arc.
257

For 1), both the εHf-εNd plot (Fig. 4a) and the $^{208}Pb/^{204}Pb$-$^{206}Pb/^{204}Pb$ plot (Fig. 4d) are effective discriminants between mantle from "Pacific' and 'Indian' mantle domains. On these plots, all FAB clearly plot well within the 'Indian' domain, a well-known characteristic of all basalts erupted within the Philippine Sea Plate (e.g. Hickey-Vargas, 1998).

For 2), the key characteristic is the decrease in εHf and $^{208}Pb/^{204}Pb$ from all FAB to axial-boninite. These features have already been identified in rocks from the nearby Bonin Ridge and attributed to the interaction of melt of 'Pacific' provenance from the newly-subducting Pacific Plate with overlying ambient mantle of 'Indian' provenance (Pearce et al., 1992; Li et al., 2013).

For 3), the key characteristic is the subsequent decrease in εNd accompanied by an increase in Sr and Pb isotope ratios from axial to off-axis boninites. This indicates the incoming of a further subduction component containing a significant contribution from Pacific Pelagic Sediment (PPS).

Fig. 4 thus highlights a remarkable variation over such a small range in space (c.15km: Fig. 1) and time (< 2m.y.: Reagan et al., 2019), and perhaps holds the key to understanding the complex and rapid evolution of ophiolite complexes believed to have a subduction initiation origin. In the Sections that follow, we interpret the trends in Fig. 4 in more detail in an attempt to establish how they may take place in the context of Western Pacific subduction initiation.

5. Interpretations

5.1 Characterizing the mantle source using εHf-εNd covariations

Applying the εHf-εNd projection (Fig. 4a) to FAB is a useful way to understand the nature and provenance of the ambient mantle at the start of subduction. Fig. 5a depicts MORB and OIB from the Western Pacific region. Our reference line is the Indian-Pacific mantle domain boundary (Pearce et al., 1999). This boundary has the equation εHf=εNd*1.6 and hence is almost parallel to, but displaced by c. 1.25 epsilon units from, the principal axis of dispersion of the global terrestrial array (εHf=εNd*1.59+1.26) of Chauvel et al. (2009). The boundary also bisects the type Pacific-Indian mantle domain boundary from the Australian-Antarctic Discordance (AAD), a long distance further to the south-east (Kempton et al., 1992).

As many authors have noted, individual lava suites commonly form arrays (termed 'ambient mantle arrays' by Woodhead et al., 2012), which typically run sub-parallel to the Pacific-Indian boundary and global terrestrial array. Behind the trench, the most relevant ambient array is that of the Philippine Sea (Fig. 5a), which began spreading at about the time of subduction initiation and continued through the evolution of the Bonin Ridge embryonic arc. Its ambient array lies well within the 'Indian' domain.

In Fig. 5b, the axial-FAB plot in the upper 50-90 percentile of the Philippine Sea MORB-OIB

array. They form an ambient FAB mantle array, which extends from E-FAB, through N-FAB to D-FAB and runs sub-parallel to other ambient mantle arrays within the Philippine Sea Plate. In contrast, the off-axis FAB form a near-vertical trend, which extends to εHf-εNd values above the Philippine Sea array.

'Indian' characteristics, such as those exhibited by Exp. 352 FAB, have been attributed to mantle depletion during a partial melting event in garnet facies (as garnet fractionates Lu from Hf, but not Sm from Nd) perhaps coupled with enrichment by a Nd-rich, Hf-poor subduction component (e.g. Kempton et al, 2002; Janney et al., 2005, Salters et al., 2011). This interpretation supports the hypothesis of Gurnis et al. (1998) that the 'Indian' domain province contains relics of subduction-modified, depleted lithosphere from a long history of sub-Gondwana subduction.

Yogodzinski et al. (2018) explore further the evolution of the mantle beneath the Philippine Sea Plate at about the time of subduction initiation by focusing on the 50-49Ma basaltic basement at Site U1438. They use plots of $^{176}Hf/^{177}Hf$ v Lu/Hf and $^{143}Nd/^{144}Nd$ v Sm/Nd to demonstrate that the mantle source experienced a long history of depletion, which includes a significant melt extraction event in the 400-500 Ma time window.

On their base diagram (Fig. 5c-d), we note that our main N-FAB magmas extend along a 52Ma errorchron in Fig. 5c, indicating fractionation of Lu/Hf during the melting event from which they formed. The D-FAB and E-FAB form two-point 195Ma and 235Ma errorchrons

for the Lu-Hf and Sm-Nd systems respectively, a potentially significant observation but one requiring further analyses. The mean N-FAB composition and the off-axis FAB plot close to the Palaeozoic errorchrons plotted by Yogodzinski et al. (2018) for IODP Site U1438: the combined basalt dataset from Sites U1438 and U1439-1442 gives similar 450Ma errorchrons on both diagrams (Fig. 5c-d), though with considerable scatter. Overall, therefore, our isotope data support the concept of Yogodzinski et al (2018) and Shervais et al. (2019) that subduction initiated within a mantle domain that had already experienced one or more ancient depletion events, though more work is needed to ascertain precise ages and details. In any event, this mantle domain provides the mantle wedge end-member needed to explain the compositions of the subsequent subduction events.

5.2 Characterizing the subduction component using isotope-element ratio covariations

Plots of the form εHf_i-x/Hf are particularly effective at interpreting Hf anomalies on the extended REE diagram (Fig. 3b-c) in terms of subduction components, as any mixing lines are then linear and so easier to interpret (e.g. Barry et al., 2006).

In Fig. 6a, x=Sm, chosen because Sm is closest to Hf in its bulk partition coefficient during mantle melting and fractional crystallization. The axial-FAB data plot at the upper (MORB) end of the ambient Philippine Sea array, while the off-axis FAB lie on an extension of this array. As can be seen in all four diagrams (Fig. 6a-d), an average axial-FAB composition is the optimum choice for the isotopic mantle end-member for the subsequent generation of boninites. Being a boninite source, this end-member is depleted in incompatible elements

346 compared to the FAB mantle source (Fig. 3) but, importantly, it is isotopically similar. We
347 term this end-member 'Residual FAB Mantle' (M in Figs 6-9).
348
349 During subduction in most active present-day arcs, Sm is more mobile than Hf. In
350 consequence, arc lavas typically lie within, or adjacent to, the high Sm/Hf (or Sm/Zr) side of
351 any MORB array (e.g. Hickey-Vargas, 1989; Barry et al., 2006). In contrast, samples from
352 the boninite sites plot towards lower Sm/Hf, reflecting their positive Hf anomalies. They have
353 been interpreted as reflecting an amphibolite-facies slab-melt component in which Sm is
354 retained by amphibole, while the slab-top temperature is high enough to dissolve sufficient
355 zircon in the slab-derived melt to release significant concentrations of Hf (Pearce et al., 1992;
356 Tollstrup et al., 2010; Li et al., 2013).
357
358 The εHf value of the first subduction component (S_1) must lie on an extension of the axial-
359 boninite trend. The minimum εHf value of the subduction component (c. 8) is the intersection
360 with the Sm/Hf axis - the value at which Sm in S_1 is negligible. The maximum value (c. 12) is
361 the lowest εHf sample of the boninite trend - the value at which mantle contribution is
362 negligible. This places the εHf value of S_1 between c.8 and c.12. This range may further be
363 constrained using the less subduction-mobile (though more compatible) element, Ti, in place
364 of Sm (Fig. 6b). This increases the minimum εHf value to c.10.7, the value at which Ti/Hf in
365 S_1 is negligible.
366
367 The location and origin of S_1 can be further constrained using experimental data and slab

368 fusion modeling. Zr/Sm ratios have been studied in particular detail for amphibolite melting
369 (Pearce et al., 1992; Foley, 2002, 2008) based on published, experimentally-derived phase
370 proportions and partition coefficients, and taking into account minor phase solubility.
371 Because Zr/Hf is not significantly fractionated during the experiments, these values convert
372 simply to Sm/Hf (Sm/Hf=c.35/(Zr/Sm)). Our best estimate for the average Sm/Hf in a
373 shallow slab melt is 0.5, which equates to a εHf value for S_1 of 11.5 (Fig. 6a). Pearce et al.
374 (1992: Fig. A2) obtain this ratio at c.900°C for water-deficient melting and c.950°C for
375 water-saturated melting.
376
377 Foley's (2002, 2008) models report these ratios as a function of degree of melting rather than
378 temperature, reaching Sm/Hf=0.5 after c.5% batch melting. In both cases, reducing
379 temperature (decreasing zircon solubility) increases Sm/Hf (decreases Zr/Sm), and hence
380 increases our εHf estimate for the slab melt. Similarly, increasing temperature decreases
381 Sm/Hf and the estimated εHf. An error bar of ±0.5 epsilon units covers the range of 800-
382 1000°C and 1-10% batch melting. Foley's mean values for eclogite melting equate to Sm/Hf
383 of 0.6 (rutile-free) to 1 (rutile-bearing), while Rapp et al. (1999, 2003) obtain Sm/Hf of 0.64
384 in one experimental charge (AB-1) for 3.8GPa and 1100°C. These values lie above the
385 empirical upper bound for εHf, therefore making deep (eclogite facies) slab melts less likely
386 than shallow (amphibolite facies) slab melts as the source of S_1.
387
388 The same approach gives a best estimate for amphibolite melts of c.500 for Ti/Hf (Fig. 6b),
389 thus supporting our εHf estimate for the S_1 end-member. In contrast, Rapp's (1999) eclogite

390 facies melting experiment gives a Ti/Hf ratio 1100, too high for eclogite facies slab melts to
391 be a likely source for S_1.
392
393 In Fig. 6c, x=Nd, allowing us to determine the Hf/Nd component ratios needed for the
394 modeling of the εHf-εNd diagram. Most of the axial-FAB samples, including D-FAB, plot in
395 the upper part of the ambient mantle array, at Nd/Hf=c. 3.6 and εHf=19. The off-axis FAB
396 are distinct in having slightly higher Nd/Hf of 4.5 and higher εHf of c. 21. The value of 11.5
397 for εHf in the slab component from Fig. 6a-b gives Nd/Hf of 1.8.
398
399 The inverse ratio, Hf/Nd, can then be used to delimit the εNd value for the subduction
400 component (Fig. 6d). The axial-boninites form a trend from residual FAB mantle (M) to
401 higher Hf/Nd. Taking the crustal end member as 0.55 (the reciprocal of Nd/Hf=1.8 from Fig.
402 6c) then gives εNd= 7.5 for the slab melt component, S_1.
403
404 Importantly, Fig. 6d also defines better the composition of the components forming the off-
405 axis boninites. The high Hf/Nd end-member of the off-axis boninite trend lies within and at
406 the lower end of the axial-boninite M-S_1 trend. We interpret this end-member as a mixture of
407 slab melt and depleted mantle, which we term hybrid mantle wedge (H). The off-axis
408 boninites extend from H towards an S_2 component at lower Hf/Nd. A projection of this trend
409 intersects the εNd axis at a value of 4 for Hf/Nd=0, making this the minimum value of εNd
410 for this component. The maximum value, the lowest analysed εNd on the trend, is 6.5.
411

412 Fig. 6d also highlights the fact that the compositions of pelagic sediments (εNd=-2 to -9) lie
413 well below the H-S_2 trend. This requires that the second subduction component (S_2) also
414 includes a high εNd component and this is most likely an altered ocean crust (AOC)
415 component. However, its εNd value is poorly defined on this projection. If it is as low at 4,
416 the AOC contribution must have a very low Hf/Nd ratio, which more typical of aqueous
417 fluid. In contrast, if it is as high as 6.5, it must have high Hf/Nd, which is more characteristic
418 of a higher temperature slab melt or supercritical fluid.
419
420 *5.3 Characterizing the subduction component using εHf-εNd covariations*
421
422 Two drill sites outboard of the IBM system (ODP Sites 801 and 1149: Fig. 1a) provide the
423 most complete isotope and element data set available for the (Jurassic) crust and sediment of
424 subducting Pacific plate and hence for interpreting the boninite site subduction components
425 (Fig. 7a).
426
427 At Site 1149, the section comprises a Pacific-MORB basement overlain by pelagic sediments,
428 the latter divided into a series of sedimentary sub-types (e.g. Plank et al., 2007; Chauvel et
429 al., 2009; Vervoort et al., 2011). Site 801 is more complex. Its oceanic crust basement
430 comprises MORB overlain by a relatively thin unit of OIB (termed 'Top Alkali Basalts', or
431 TAB) (Hauff et al, 2003). The pure basalt compositions form an ambient mantle trend well
432 within the Pacific Field in Fig. 7a. However, the composites, made up of interstitial materials
433 in addition to lavas, are displaced to lower εNd and plot close to the Indian-Pacific boundary.

434 In addition to pelagic sediments, the Site 801 sedimentary section contains volcanogenic
435 sediments resulting from Jurassic intraplate magmatism. Plotted on Fig. 7a are a series of
436 component mixing hyperbolae for Sites 1149 and 801 based on these published compositions.
437 Bulk subducted compositions for Sites 1149 and 801 should plot on the bulk crust - bulk
438 sediment curves A and D respectively.
439
440 In Fig. 7b, we plot the Exp. 352 data together with the subduction components S_1 and S_2
441 inferred from Fig. 6. The obvious interpretation is that component S_1 lies between Site 801
442 MORB and TAB composites (i.e. along trend B on Fig. 7a). Component S_2 lies on the trend
443 from the inferred hybrid mantle wedge (H) and subducted Site 801 sediment (pelagic +
444 volcanogenic). A model based on the Site 801 section can therefore best explain the
445 components produced at the start of subduction.
446
447 Fig. 7c focuses on mixing models for M-S_1 and H-S_2. The former has been constructed using
448 a standard mixing equation with Nd/Hf ratios obtained from the εHf-Nd/Hf and εNd-Hf/Nd
449 plots (Pearce et al., 1999). We use axial-FAB to define the isotopic composition of residual
450 FAB mantle (M), as in Fig. 6.
451
452 Mantle: E-FAB source (for trend 3: $\varepsilon Nd_M=7.8$; $\varepsilon Hf_M=18$; $Nd/Hf)_M=4.3$
453 Mantle N-FAB source (for trend 4): $\varepsilon Nd_M=8.8$; $\varepsilon Hf_M=19.5$; $Nd/Hf)_M=3.6$
454 Mantle: D-FAB source: (for trend 5): $\varepsilon Nd_M=9.7$; $\varepsilon Hf_M=21$; $Nd/Hf)_M=3.8$
455 Subduction component (S_1='Pacific' slab melt): $\varepsilon Nd_{S1}=7.5$; $\varepsilon Hf)_{S1}=11.5$; $Nd/Hf)_{S1}=1.8$

456

457 It is apparent from resulting mixing hyperbolae (Fig. 7c, trends 3-5) that the trends from
458 axial-FAB to S_1 encompass almost all of the axial-boninite data, so supporting the concept
459 that the axial-boninites are the product of mixing of 'Pacific' crustal slab melt and the
460 ambient 'Indian' mantle source. To annotate the hyperbolae in terms of mass fractions of
461 subduction zone components requires a knowledge not just of ratios but also of the absolute
462 values of $Nd)_M/Nd)_{S1}$ or $Hf)_M/Hf)_{S1}$. Because these are not well constrained, we plot mixing
463 lines as hyperbolae for the particular optimum value of r, where $r = (Nd/Hf)_M/(Nd/Hf)_{S1}$. For
464 example, the value of r for Trend 4 is then 3.6/1.8=2.0.

465

466 Note that it is very rare to be able to define mantle-slab melt mixture so clearly; it is only
467 possible here because of the distinction between 'Indian' provenance mantle and 'Pacific'
468 provenance crust and the absence of a large sediment component. Most Western Pacific arcs
469 are cooler and mixing lines run between 'Indian' mantle and pelagic sediment. Notable
470 exceptions are in the rear-arc volcanoes (e.g. Tollstrup et al., 2010), which lie above deeper,
471 and hence hotter, slabs.

472

473 To model the off-axis boninite variations, we continue to infer that they involve the mixing of
474 mantle already containing the slab melt component (the hybrid mantle wedge, H) and an
475 added subduction component (S_2) with lower εNd made up of a mixture of a sediment-
476 derived component and an AOC-derived component. Here, we base our model on the lower
477 temperature S_2 end-member from the H-S_2 trend in Fig. 6d, made up of an AOC component

478 with Hf/Nd=c.0 and a pelagic sediment component with Hf/Nd=c. 0.5. Values used are:

479

480 Hybrid (slab melt-modified) residual mantle (H): εNd_M=8.0; εHf_M=12; $Nd/Hf)_M$=1.8

481 Additional subduction component (S_2): εNd_{S2}=4.0; εHf_{S2}=12; $Nd/Hf)_{S2}$=20

482

483 In fact, Fig. 6d showed that this S_2 could have εNd as high as 6.5, although this higher value
484 would have little effect on the general interpretation. We can, however, constrain this
485 component further by incorporating isotopes of Pb and Sr, which partition more readily than
486 Nd and Hf into crust-derived fluids and sediment-derived fluids and melts (Fig 8).

487

488 *5.4 Identifying and tracing subduction sources during subduction initiation using plots of*
489 *isotope ratios v Δ8/4*

490

491 In Fig. 8, we plot εHf, εNd, $^{87}Sr/^{86}Sr$ and $^{207}Pb/^{204}Pb$ against Δ8/4, where Δ8/4 is the
492 orthogonal deviation from the Northern Hemisphere Reference Line (NHRL) in $^{208}Pb/^{204}Pb$-
493 $^{206}Pb/^{204}Pb$ space, as defined by Hart (1984) (Fig. 4d). In all the plots, we can recognize the
494 two subduction components that were apparent in the Hf-Nd projections. For the purpose of
495 this paper (the tracing of mantle and subduction components following subduction initiation),
496 we continue to interpret these trends in terms of simple mixing of two end members, but
497 realise that this is an approximation given the complex nature of the mantle wedge.

498

499 The first trend, as modeled in Fig. 7, marks the addition of 'Pacific' slab melt (S_1) to 'Indian'

500 Residual FAB Mantle (M). Given that the εNd value of this component was established at c.
501 7.5, we can use Fig. 8b to fix the S_1 component at Δ8/4=c.-30, i.e. in the expected field of
502 Pacific altered oceanic crust (AOC).
503
504 The second trend runs from the hybrid mantle wedge (H) to S_2. S_2 cannot be precisely
505 defined, but constraints are sufficient to demonstrate that AOC and pelagic sediments are its
506 principal contributors. First, an extrapolation of the linear regression in Figure 8d places S_2
507 on a line between H and the pelagic sediment field. As we inferred from Fig. 6d that the εNd
508 of S_2 lies between 4 and 6.5, this in turn ties Δ8/4 to a value between c.5 and 20, some way
509 from being pure pelagic sediment. Thus, S_2 requires a combination of AOC and Pacific
510 pelagic sediment (PPS), possibly with some volcanogenic sediment. The former could have
511 the same isotopic composition as S_1 if it was derived from the same subducted basalt as that
512 supplying the slab melt for the axial-boninites. Changing the εNd value of S_2 changes the
513 ratio of these components but not the nature and composition of the end-members.
514
515 The elemental concentrations of Nd, Hf and Sr relative to Pb in S_1 and S_2 may be gleaned
516 from the curvatures of the axial and off-axis boninite trends respectively. These shapes of the
517 mixing hyperbolae are a function of the ratios r_1 $[(x/Pb)_M/(x/Pb)_{S1}]$ and r_2 $[(x/Pb)_H/(x/Pb)_{S2}]$
518 where x=Hf, Nd or Sr. These shapes match the patterns in Fig. 3, by indicating that S_1
519 contains high Pb and Sr, significant Hf and relatively little Nd and that S_2 carries further Pb
520 and Sr but undetectable Hf and significant Nd. As already discussed, S_1 can be explained by
521 residual amphibole during slab melting, S_2 by the incoming of pelagic sediment.

6. Discussion: isotopic constraints on magma genesis following subduction initiation

Fig. 9 presents a conceptual model that we believe best satisfies the isotopic constraints derived from this study. Further details and discussion of this model are given below.

6.1 Constraints from the absence of a subduction component in the axial fore-arc basalts (Sites U1440 and U1441)

The FAB drilled at IODP Exp. 352 Sites U1440 and U1441 show no clear isotopic evidence for a subduction component. There are therefore two principal modes of origin: spreading immediately after subduction; or spreading immediately before subduction. Both models are consistent with the 'Indian' character of the ambient mantle given that the position of the 'Pacific-Indian' mantle domain boundary lay outboard of the transform plate boundary (Miyazaki, 2015) and would have been sampled in either case. Based on regional-scale sampling, however, Reagan et al. (2010) find that subduction-free FAB similar to that drilled during Exp. 352 comprises one end-member of a spectrum that extends to FAB with clear subduction enrichment. From this, they conclude that spreading following subduction was the more likely, i.e. that extension was due to slab roll-back as proposed by Stern and Bloomer (1992). In that case, rapid mantle upwelling relative to the rate of heating of the slab is required to minimize the subduction input of the subduction-free end-member compositions.

544

545 *6.2 Constraints from the shallow slab-melting component in the axial-boninites (Holes*
546 *U1439C and U1442A)*

547

548 The isotopic evidence presented here supports a model in which the axial-boninite sources
549 are the products of variable interaction between ambient, 'Indian' domain, residual FAB
550 mantle and shallow, amphibolite facies, slab melts (S_1). These shallow slab melts are likely
551 tonalitic in composition, lacking the depletion in heavy REE relative to middle REE of
552 deeper (adakitic) slab melts. This model is similar to that developed for boninites in the
553 Bonin Ridge and its northward extension (Pearce et al., 1992; Li et al, 2013). However, our
554 boninites from Exp. 352 are older than the Bonin Ridge boninites (c. 51Ma versus c. 46Ma),
555 so providing the first evidence that shallow slab melting started very soon after subduction
556 initiation before continuing for at least 5 m.y. Early slab melting is consistent with thermal
557 models, where the first crust to subduct melts at shallow depths because it encounters mantle
558 uncooled by subsequent subduction (Pearce et al., 1992).

559

560 An alternative model that can be ruled out is the basalt melt contributing to S_1 was not the
561 product of slab melting, but instead was derived from fusion of basalt (FAB) veins within the
562 mantle wedge (Pearce et al., 1999). This model was put forward to explain the genesis of
563 ODP Leg 125 boninites, where both end-members of the equivalent M-S_1 trend lie within the
564 'Indian domain'. In this study, S_1 has a clear 'Pacific' provenance, so strongly supporting the
565 slab-melt model.

566

567 It is significant that our new data effectively rule out two previous models for the origin of
568 the slab melts. Casey and Dewey's (1984) model of a leaky transform fault attributes slab
569 melting to subduction of ridges within the transform zone. If true, the spreading ridges would
570 need to lie within the 'Pacific' mantle domain. However, isotopic studies of accreted basalts
571 show that the Izanagi-Pacific Ridge had crossed a static 'Indian-Pacific' mantle domain
572 boundary by 80m.y. (Miyazaki et al., 2015) and thus that the present boundary lies beneath
573 the Pacific plate. In fact, Straub et al. (2015) found that oceanic crust of 'Indian' provenance
574 did become the source of subduction components within the Izu-Bonin system, but not until
575 at least 10 m.y. after subduction initiation. The same arguments negate the likelihood of
576 larger-scale ridge subduction events being the cause of boninite magmatism (Seton et al.,
577 2015).

578

579 *6.3 Start of sediment input and the origin of the off-axis boninites (Holes U1439C and*
580 *U1442A Upper lava Units)*

581

582 A key question arising from Section 5 is why sediment input begins between the eruption of
583 axial-boninites and the eruption of off-axis boninites. There are at least three possibilities: 1)
584 a sediment component is also present in S_1 but is swamped by the slab melt signal; 2) the first
585 subducted crust originated in a transform zone where deeper sea-floor, less high-temperature
586 hydrothermal activity and more detachment faulting resulted in minimal sedimentary cover;
587 and 3) the sediment is initially accreted rather than subducted. The argument against first

588 option is that Pb isotopes proved highly sensitive to the sediment content of S_2, and so would
589 have detected a sediment component in S_1 were it present in significant proportion. The
590 second option cannot be ruled out, but transform faults are rarely sediment-free and often
591 contain debris flows made up of igneous clasts in sediment matrices, which would contribute
592 a sedimentary signal to the subduction component. Thus, we consider the accretionary option
593 to be most likely.
594
595 In the accretionary model, sediments would have to be accreted at the start of subduction so
596 that the slab that initially rolls back is sediment free. For this to happen, subduction dynamics
597 must change between the input of S_1 and S_2 in a way that first inhibits sediment subduction
598 and then permits it. Critical taper theory (e.g. Dahlen, 1990) supported by subduction zone
599 comparisons (Clift and Vannucchi, 2004) reveal that shallow and slow subduction favor
600 development of accretionary margins and hence off-scraping of sediment, while steep and
601 fast subduction favor non-accretionary margins and hence sediment subduction.
602
603 In Fig 9 (a) subduction starts slowly and at a shallow angle up to the point at which oceanic
604 crust converts to eclogite, after which (b) rapid roll-back takes place of the sediment-free
605 subducting slab culminating in addition of S_1, followed by (c) normal, rapid and steep
606 subduction (likely with a roll-back component) in which the accreted sediment in able to
607 subduct. Introduction of fluid and/or melt from sediment and AOC (S_2), either separately or
608 together as a mélange with altered basaltic debris (Nielsen and Marschall, 2017), then allows
609 the sub-solidus hybrid mantle wedge to undergo the additional hydration to produce the off-

axis boninites trench-side of the original ridge.

7. Conclusions

1. The first stage of magmatism following subduction initiation is associated with sea-floor spreading following subduction initiation and results in the eruption of forearc basalts (FAB) at IODP Sites U1440 and U1441. Isotope data confirm that these FAB lack a subduction component and so can be used to characterize the ambient mantle reservoir prior to the input of the subduction component. Notably, this reservoir had 'Indian' provenance and had experienced an ancient (possibly Palaeozoic), garnet facies depletion event, similar to that proposed by Yogodzinski et al. (2018) based on the slightly younger, and more trench-distal, basalts drilled at IODP Site U1438.

2. The first evidence of subduction is recorded by the axial boninites at IODP Sites U1439 and U1442. Their isotopic compositions follow mixing trends between residual mantle of 'Indian' provenance and oceanic crust of 'Pacific' provenance. The latter had undergone shallow (amphibolite facies) fusion to give positive Hf anomalies on extended REE plots, so providing further evidence for slab fusion at the start of subduction. The absence of sediment in the isotope signal may be explained by initial sediment accretion, although other options are possible.

3. The final stage is the eruption of the off-axis boninites. Their isotopic compositions follow

632 mixing trends between a hybrid mantle wedge similar to the axial boninite source (slab melt
633 plus residual mantle) and a subduction component derived from altered oceanic crust (AOC)
634 and Pacific pelagic sediment (PPS). Our favored explanation for the sudden appearance of the
635 sediment component is subduction of previously accreted material resulting from increased
636 subduction rate and slab dip. As this event takes place <2m.y after the genesis of the forearc
637 basalts (Reagan et al., 2019), the results provide evidence that subduction initiation was
638 followed by a rapidly evolving system in terms of geodynamics, magma genesis and crustal
639 accretion.
640
641 **Acknowledgements**
642
643 We thank the International Ocean Discovery Program (IODP) for samples and infrastructure.
644 We appreciate the contributions of the Staff Scientist (K. Petronotis) and remaining members
645 of the IODP Exp. 352 Scientific Party as well as the officers and crew, and scientific support
646 staff, on the JOIDES Resolution. We thank Gene Yogodzinski and an anonymous referee for
647 their helpful recommendations and Tamsin Mather for her editorial support. Hong-Yan Li
648 additionally thanks the Strategic Priority Research Program of the Chinese Academy of
649 Sciences (Grant No. XDB18000000) and the National Programme on Global Change and
650 Air-Sea Interaction (GASI-GEOGE-02). Shervais, Ryan and Reagan thank the USSSP for
651 initial Expedition funding and the NSF for grants OCE1558689, OCR1558855 and
652 OCE1558647 respectively. Taylor & Pearce and Prytulak thank the NERC (UK) for grants
653 NE/M012034/1 and NE/M010643 respectively. Godard thanks CNRS-INSU Terre Solide

654 ‘Soutien Post-campagne à la Mer’. Hong-Yan Li thanks Xiang Li, Le Zhang and Jinlong Ma
655 for their contributions to the analyses in GIGCAS laboratories. Prytulak thanks K. Kressig,
656 B.J. Coles, M. Mangler and F. Wei for their contributions to the analyses and running of the
657 MAGIC laboratories. This is contribution No. IS–2640 of GIG-CAS
658

659 **Appendix A and B. Supplementary material**

660

661 Supplementary material related to this article can be found on-line at
662 https://doi.org/10.1016/…..

663

664 **References**

665

666 Barry, T., Pearce J.A., Leat, P.T., Millar, I.L., 2006. Hf isotope evidence for selective
667 mobility of high-field-strength-elements in a subduction setting: South Sandwich Islands,
668 Earth Planet. Sci. Lett. 252, 223-244.

669 Casey, J. F., Dewey, J. F., 1984. Initiation of subduction zones along transform and accreting
670 plate boundaries, triple-junction evolution and forearc spreading centres - implications for
671 ophiolitic geology and obduction. Geol. Soc. Lond. Spec. Publ. 13, 269-290.

672 Chauvel, C., Marini, J.-C., Plank, T., Ludden, J., 2009. Hf-Nd input flux in the Izu-Mariana
673 subduction zone and recycling of subducted material in the mantle. Geochem. Geophys.
674 Geosyst. 10, Paper Number 2008GC002101.

675 Clift, P., Vannucchi, P., 2004. Controls on tectonic accretion versus erosion in subduction
676 zones: implications for the origin and recycling of the continental crust. Rev. Geophys. 42,
677 RG2001, doi:10.1029/2003RG000127.

678 Cosca, M.A., Arculus, R.J., Pearce, J.A., Mitchell, J.G., 1998. $^{40}Ar/^{39}Ar$ and K-Ar
679 geochronological age constraints for the inception and early evolution of the Izu-Bonin arc
680 system. Island Arc. 7, 579-595.

681 Crawford, A.J. ed., 1989. Boninites and related rocks. London (Unwin Hyman) 465 pp.

682 Dahlen, F. A., 1990. Critical taper model of fold-and-thrust belts and accretionary wedges.
683 Ann. Rev. Earth Planet. Sci.18, 55-99.

684 Dilek, Y., Flower, M.F.J., 2003. Arc-trench rollback and forearc accretion; 2, A model
685 template for ophiolites in Albania, Cyprus, and Oman: Geol. Soc. Spec. Publ. 218, 43-68.

686 Foley, S., Tiepolo, M., Vannucci, R., 2002. Growth of early continental crust controlled by
687 melting of amphibolite in subduction zones. Nature 417, 837-840.

688 Foley, S., 2008. A trace element perspective on Archean crust formation and on the presence
689 or absence of Archean subduction. Geol. Soc. Amer. Spec. Pap. 440, 31-50.

690 Gale, A., Dalton, C.A., Langmuir, C.H., Su, Y., Schilling, J.-G., 2013. The mean composition
691 of ocean ridge basalts. Geochem. Geophys., Geosyst. 14, 489-518.

692 Gurnis, M., Müller, R. D., Moresi, L., 1998. Cretaceous vertical motion of Australia and the
693 Australian–Antarctic Discordance. Science 279, 1499–1504.

694 Hart, S.R., 1984. A large-scale isotope anomaly in the Southern Hemisphere mantle. Nature
695 309, 753-757.

696 Hauff, F., Hoernle, K., Schmidt, A., 2003. Sr-Nd-Pb composition of Mesozoic Pacific
697 oceanic crust (Site 1149 and 801, ODP Leg 185): implications for alteration of ocean crust
698 and the input into the Izu-Bonin-Mariana subduction system. Geochem. Geophys. Geosyst. 4,
699 Paper No. 2002GC000421.

700 Heydolph, K., Murphy, J., Geldmacher, J., Romanova, I.V., Greene, A., Hoernle, K., Weis,
701 D., Mahoney, J., 2014. Plume versus plate origin for the Shatsky Rise oceanic plateau
702 (NWPacific): insights from Nd, Pb and Hf isotopes. Lithos 200-201, 49-63.

703 Hickey-Vargas, R., 1989. Boninites and tholeiites from DSDP Site 458, Mariana forearc. In
704 Crawford, A. J. (Ed.), Boninites and Related Rocks: London (Unwin Hyman), 339-356.

705 Hickey-Vargas, R., 1998. Origin of the Indian Ocean-type isotopic signature in basalts from
706 Philippine Sea plate spreading centers: an assessment of local versus large-scale processes. J.
707 Geophys. Res. 103, 20,963-20,979.

708 Hussong, D. M., Uyeda, S., 1981. Tectonic processes and the history of the Mariana arc: a
709 synthesis of the results of Deep Sea Drilling Project Leg 60. In: Hussong, D. M., Uyeda, S.,
710 et al., Init. Repts. DSDP, 60: Washington (U.S. Govt. Printing Office), 909-929.

711 Ishizuka, O., Tani, K., Reagan, M.K., Kanayama, K., Umino, S., Harigane, Y., Sakamoto, I.,
712 Miyajima, Y., Yuasa, M., Dunkley, D.J., 2011. The timescales of subduction initiation and
713 subsequent evolution of an oceanic island arc: Earth Planet. Sci. Lett. 306, 229-240.

714 Ishizuka, O., Hickey-Vargas, R., Arculus, R.J, Yogodzinski, G.M., Savov, I.P., Kusanoa, Y.,
715 McCarthy, A., Brandl, P.A., Sudoi, M., 2018. Age of Izu–Bonin–Mariana arc basement,
716 Earth Planet. Sci. Lett. 481, 80-90.

717 Janney, P.E., Le Roex, A.P., Carlson, R.W., 2005. Hafnium isotope and trace element
718 constraints on the nature of mantle heterogeneity beneath the central Southwest Indian Ridge
719 (13°E to 47°E). J. Petrol. 46, 2427-2464.

720 Kempton, P. D., Pearce, J. A., Barry, T. L., Fitton, J. G., Langmuir, C., Christie, D. M., 2002.
721 Sr–Nd–Pb–Hf isotope results from ODP Leg 187: evidence for mantle dynamics of the
722 Australian–Antarctic Discordance and origin of the Indian MORB source. Geochem.
723 Geophys. Geosyst. 3, Paper No. 2002GC000320.

724 Leng, W., Gurnis, M., Asimow, P., 2012. From basalts to boninites; the geodynamics of
725 volcanic expression during induced subduction initiation. Lithosphere 4, 511-523.

726 Li, Y.-B., Kimura, J.-I., Machida, S., Ishii, T., Ishiwatari, S., Maruyama, S., Qiu, N.-N.,
727 Ishikawa, T., Kato, Y., Haraguchi, S., Takahata, N., Hirahara, Y., Miyazaki, T., 2013. High-
728 Mg adakite and low-Ca boninite from a Bonin fore-arc seamount: implications for the
729 reaction between slab melts and depleted mantle. J. Petrol 54, 1149-1175.

730 Macpherson, C.G., Hall, R., 2001. Tectonic setting of Eocene boninite magmatism in the Izu-
731 Bonin-Mariana forearc. Earth Planet. Sci. Lett. 186, 215-230.

732 Miyazaki, T., Kimura, J.-I., Senda, R. et al., 2015. Missing western half of the Pacific Plate:
733 Geochemical nature of the Izanagi-Pacific Ridge interaction with a stationary boundary

734 between the Indian and Pacific mantles. Geochem., Geophys., Geosyst. 16, 3309-3332,
735 doi:10.1002/2015GC005911.

736 Nielsen, S.G., Marschall, H.R., 2017. Geochemical evidence for mélange melting in global
737 arcs. Sci. Adv. 3, e1602402.

738 Niu, Y., O'Hara, M.J., Pearce, J.A., 2003. Initiation of subduction zones as a consequence of
739 lateral compositional buoyancy contrast within the lithosphere: a petrological perspective. J.
740 Petrol. 44, 851-866.

741 Pearce, J.A., van der Laan, S.R., Arculus, R.J., Murton, B.J., Ishii, T., Peate, D.W.,
742 Parkinson, I., 1992. Boninite and harzburgite from Leg 125 (Bonin-Mariana Forearc): a case
743 study of magma genesis during the initial stages of subduction, Proceedings of the Ocean
744 Drilling Program Scientific Results, v. 125, p. 623-659.

745 Pearce, J. A., Kempton, P. D., Nowell, G. M., Noble, S. R., 1999. Hf–Nd element and isotope
746 perspective on the nature and provenance of mantle and subduction components in western
747 Pacific arc–basin systems. J. Petrol. 40, 1579-1611.

748 Plank, T., Kelley, K.A., Murray, R.W. and Stern, L.Q., 2007. Chemical composition of
749 sediments subducting at the Izu-Bonin trench. Geochem., Geophys. Geosyst. 8, Paper No.
750 2006GC001444.

751 Rapp, R.P., Shimizu, N., Norman, M.D., Applegate, G.S., 1999. Reaction between slab-
752 derived melts and peridotite in the mantle wedge: experimental constraints at 3.8 GPa. Chem.
753 Geol. 160, 335-356.

754 Rapp, R.P., Shimizu, N., Norman, M.D., 2003. Growth of early continental crust by partial
755 melting of eclogite. Nature 425, 605-609.

756 Reagan, M.K., Heaton, D.E., Schmitz, M.D., Pearce, J.A., Shervais, J.W., and Koppers, A.A.
757 P., 2019. Forearc ages reveal extensive short-lived and rapid seafloor spreading following
758 subduction initiation: Earth Planet. Sci. Lett. 506, 520-529.

759 Reagan, M.K., Ishizuka, O., Stern, R.J., Kelley, K.A., Ohara, Y., Blichert-Toft, J., Bloomer,
760 S.H., Cash, J., Fryer, P., Hanan, B., Hickey-Vargas, R., Ishii, T., Kimura, J.-I., Peate, D.W.,
761 Rowe, M. C., Woods, M., 2010. Fore-arc basalts and subduction initiation in the Izu-Bonin-
762 Mariana system. Geochem. Geophys. Geosyst. 11, 1-17.

763 Reagan, M.K., Pearce, J.A., Petronotis, K., Almeev, R.R., Avery, A.J., Carvallo, C., Chap-
764 man, T., Christeson, G.L., Ferré, E.C., Godard, M., Heaton, D.E., Kirchenbaur, M., Kurz, W.,
765 Kutterolf, S., Li, H., Li, Y., Michibayashi, K., Morgan, S., Nelson, W.R., Prytulak, J.,
766 Python, M., Robertson, A.H.F., Ryan, J.G., Sager, W.W., Sakuyama, T., Shervais, J.W.,
767 Shimizu, K., Whattam, S.A., 2017. Subduction initiation and ophiolite crust: new insights
768 from IODP drilling. Int. Geol. Rev. 59. https://doi .org /10 .1080 /00206814 .2016 .1276482.
769

770 Reagan, M.K., Pearce, J.A., Petronotis, K.E., and the Expedition 352 Scientists, 2015.
771 Expedition 352 summary. Proc. IODP Volume 352. doi:10.14379/iodp.proc.352.101.2015.

772 Salters, V.J.M., Mallick, S., Hart, S.R., Langmuir, C.E., Stracke, A., 2011. Domains of
773 depleted mantle: New evidence from hafnium and neodymium isotopes. Geochem. Geophys.
774 Geosyst. 12, Paper No. GC003617.

775 Savov, I.P., Hickey-Vargas, R., D'Antonio, M., Ryan, J.G., Spadea, P., 2006. Petrology and
776 geochemistry of West Philippine Basin Basalts and early Palau–Kyushu arc volcanic casts
777 from ODP Leg 195, Site 1201D: implications for the early history of the Izu–Bonin–Mariana
778 Arc. J. Petrol. 47, 277-299.

779 Seton, M., Flament, N., Whittaker, J., Muller, D., Gurnis, M., Bower, D.J., 2015. Ridge
780 subduction sparked reorganization of the Pacific plate- mantle system 60–50 million years
781 ago. Geophys. Res. Lett. 42, https://doi.org/10.1002/2015GL063057.

782 Shervais, J.W., 2001. Birth, death, and resurrection: The life cycle of suprasubduction zone
783 ophiolites. Geochem. Geophys. Geosyst. 2, Paper number 2000GC000080.

784 Shervais, J.W., Reagan, M.K., Haugen, E., Almeev, R.R., Pearce, J.A., Prytulak, J., Ryan,
785 J.G., Whattam, S.A., Godard, M., Chapman, T., Li, H.-Y., Kurz, W., Nelson, W.R., Heaton,
786 D.E., Kirchenbaur, M., Shimizu, K., Sakuyama, T., Li, Y., and Vetter, S.K., 2019. Magmatic
787 response to subduction initiation: Part 1. Fore-arc basalts of the Izu-Bonin arc from IODP
788 Expedition 352: Geochem. Geophys. Geosyst. 20, https://doi.org/10.1029/2018GC007731.

789 Stern, R.J., and Bloomer, S.H., 1992, Subduction zone infancy; examples from the Eocene
790 Izu-Bonin-Mariana and Jurassic California arcs: Geological Society of America Bulletin,
791 104, 1621-1636.

792 Straub, S. M., J. D. Woodhead, J.D. Arculus, R.J., 2015. Temporal evolution of the Mariana
793 Arc: Mantle wedge and subducted slab controls revealed with a tephra perspective, J. Petrol.
794 56, 409–439, doi:10.1093/petrology/egv005

795 Sun, S. S., McDonough, W. F., 1989. Chemical and isotopic systematics of oceanic basalts:
796 implications for mantle composition and processes. Geol. Soc. Lond. Spec. Publ. 42, 313-
797 346.

798 Tollstrup, D.L., Gill, J.B., Kent, A., Prinkey, D., Williams, R., Tamura, Y., Ishizuka, O.,
799 2010. Across-arc geochemical trends in the Izu-Bonin arc: contributions from the subducting
800 slab, revisited. Geochem. Geophys. Geosyst. 11, Paper no. 2009GC002847.

801 Vervoort, J.D., Plank, T., Prytulak, J., 2011. The Hf–Nd isotopic composition of marine
802 sediments. Geochim. Cosmochim. Acta 75, 5903-5926.

803 Woodhead, J., Stern, R.J., Pearce, J., Hergt, J., Vervoort, J., 2012. Hf-Nd isotope variation in
804 Mariana Trough basalts: The importance of "ambient mantle" in the interpretation of
805 subduction zone magmas. Geology. 40, 539-542.

806 Wu, W., Suppe, J., Lu, R., Kanda, R., 2016. Philippine Sea and East Asian plate tectonics
807 since 52Ma constrained by new subducted slab reconstruction methods. J. Geophys. Res.
808 Solid Earth 121, 4670-4741.

809 Yogodzinski, G., Bizimis, M., Hickey-Vargas, R., McCarthy, A., Hocking, B.D., Savov, I.P.,
810 Ishizuka, O., Arculus, R., 2018. Implications of Eocene-age Philippine Sea and Forearc
811 basalts for initiation and early history of the Izu-Bonin-Mariana arc. Geochem. Cosmochim.
812 Acta. doi: fttps://doi.org/10.1016/j.gca.2018.02.047.

813

814 Table Caption

815 Table 1. Representative isotope analyses from fore-arc basalt IODP Exp. 352 Holes
816 U1440B and U1441A, and boninite Holes U1439C and U1442A. For locations, see
817 Fig. 1. For the full data table, including major and trace element analyses and errors,
818 see Appendix A. For full analytical details, see Appendix B. For Pb and Sr isotope
819 analyses: the four samples marked by asterisks in the Table were separates of fresh
820 glasses collected close to Hf-Nd sample locations; non-glass samples that gave non-
821 reproduceable Pb isotope ratios despite heavy leaching are marked as 'altered'. Rock
822 type abbreviations: FAB= Forearc Basalt (D= depleted; N= Normal, E= enriched);
823 LSB= Low-Si Boninite; HSB= High-Si Boninite; HMA= High-Mg Andesite. All
824 samples are lavas except U1440B Unit 15 and U1439C Unit 10, both of which are
825 sheeted intrusions (superscript D).

826

827

828 Figure Captions

829

830 Figure 1. Location and geological setting of the IODP Exp. 352 drill sites in the Bonin
831 forearc, Western Pacific (modified from Reagan et al., 2015). (a) Location relative to
832 key geographic features and drill sites. (b) Geological setting of the four drill sites.
833 Sites U1440 and U1441 are the 'FAB sites', and Sites U1439 and U1442 are the
834 slightly younger and more trench-distal 'boninite sites'. Base map from submersible
835 sampling and dredging coupled with age dating (Reagan et al., 2010; Ishizuka et al.,
836 2011). (c) Simplified logs for the four principal basement-penetrating holes from the
837 FAB and boninite sites. Modified from Reagan et al. (2017) with ages from Reagan et
838 al. (2019). FAB=forearc basalt; LSB=low-Si boninite; HSB=high-Si boninite;
839 HMA=high-Mg andesite.

840

841 Figure 2. Isotope stratigraphies for the FAB sites (Holes 1440B and U1441A) and
842 boninite sites (Holes U1439C and U1442A). Both of the FAB and boninite
843 stratigraphies may be subdivided into axial (lower) and off-axis (upper) groups. The
844 axial-FAB subdivide on trace element criteria into D(depleted)-FAB, the dominant
845 N(normal)-FAB and E(enriched)-FAB: these differ in εNd_i values, which increase
846 from D- through N-FAB to E-FAB. Off-axis FAB have distinctly lower εNd_i than
847 axial-FAB, and off-axis boninites mostly have lower εNd_i and εHf_i than axial-
848 boninites as well as higher $^{206}Pb/^{204}Pb$ isotope ratios. All FAB have higher εHf_i and
849 lower $^{206}Pb/^{204}Pb$ than all boninites. Note that the Pb analysis in parentheses is

anomalous (off-axis composition in an axial sequence), which may indicate fluid-flux from above, and so is omitted from later diagrams. mbsf=meters below sea-floor.

Figure 3. Extended chondrite-normalized REE plots highlighting the changes in the radiogenic daughter isotope elements, Pb, Sr, Nd and Hf during the evolution from (a) axial- and off-axis FAB through (b) axial-boninites to (c) off-axis boninites. Note the absence of significant subduction-related anomalies in the FAB (the alteration-related Sr anomaly in the D-FAB sample has been omitted), in contrast to the positive Pb, Sr and Hf anomalies in the boninites. Note also that the LREE (and hence Nd) progressively increase from FAB through axial boninite to off-axis boninite, as seen in the trend from LREE-depleted to slight LREE enrichment. Chondrite-normalizing factors are from Sun and McDonough (1989), with the Pb value amended to remove the metallic component of the chondrite. For full elemental analyses, see Appendix A.

Figure 4. Standard Nd, Hf, Sr and Pb isotope projections, showing the isotopic evolution of magmatism from axial-FAB through off-axis FAB through axial-boninite to off-axis boninite. Principal features, investigated in more detail using Figures 5-8, are: 1) an increase in εHf_i from axial-FAB to off-axis-FAB; 2) a decrease in εHf_i, and Pb isotope ratios from FAB to axial-boninites; and 3) a decrease in εNd_i coupled to an increase in Sr and Pb isotope ratios from axial to off-axis boninites. The general explanations for these observations are respectively: for 1), the arrival of a long-term depleted mantle source for the off-axis FAB; for 2), incoming of a subduction component derived from fusion of 'Pacific' domain, altered oceanic crust (AOC) for the axial boninites and for 3), incoming of a further subduction component containing

874 a significant contribution of Pacific Pelagic Sediment (PPS) for the off-axis boninites.
875 This is a remarkable variation for such small differences in space and time.

876

877 Figure 5. Isotopic interpretations of FAB used to establish mantle compositions
878 immediately following subduction initiation. (a) Contrast in 'Pacific' and 'Indian'
879 mantle sources in the Western Pacific and Australian-Antarctic Discordance (AAD).
880 #801, #1149, #1438 refer to drill core from ODP Leg 129 Site 801, ODP Leg 185 Site
881 1149 and IODP Exp. 351 Site U1438 respectively (see Fig. 1 for locations). Data are
882 from Chauvel et al. (2009), Heydolph et al. (2014), Hickey-Vargas (1998), Miyazaki
883 et al. (2015), Pearce et al., (1999), Savov et al. (2006) and Yogodzinski et al. (2018).
884 (b) Plot of Exp. 352 FAB data, demonstrating that the axial-FAB plot within the
885 Philippine Sea 'Indian' mantle array in a similar position to Site U1438 Unit 1e, while
886 the off-axis FAB lie above this array. Fig. 5c-d explore the nature of Exp. 352 FAB
887 mantle sources, taking as base diagrams the plots of Yogodzinski et al. (2018) for Site
888 U1438 Units a-e, the closest lavas from the Philippine Sea in space (at the time of
889 eruption) and time. The plots indicate that Lu/Hf fractionation during mantle melting
890 likely explains the variations within N-FAB, and that the isotopic variations from E to
891 N to D-FAB within axial-FAB, and those within off-axis FAB, likely require older
892 (possibly both Mesozoic and Palaeozoic) enrichment and depletion events. Note that
893 boninites have not been plotted because Hf and Nd are both subduction-mobile (Fig.
894 3). The AAD field marks the compositions of lavas transitional between Indian and
895 Pacific provenance along the Australian-Antarctic Ridge.

896

Figure 6. Use of εHf-x/Hf and εNd-y/Nd plots (where x is Sm, Ti or Nd and y is Hf) to constrain the εHf and εNd values of mixing end-members. The diagrams help define two trends: the first from M (residual FAB mantle) and a shallow (amphibolite-facies) slab melt (at S_1); and the second from a point on that trend representing a hybrid mantle wedge (H) to a component containing pelagic sediment and an altered oceanic crust (AOC) component (at S_2). Data sources for the ambient (Philippine Sea) mantle array are given in the caption to Fig. 5. The gradient of the ambient mantle array reflects the difference in incompatibility between x and Hf or Nd (positive if x is less compatible).

Figure 7. Modeling of the εHf-εNd covariation diagram in Fig. 4a. Fig. 7a summarizes published data for potential subducted materials from the Sites 801 and 1149 (Fig. 1a). Basement composites (subscript C) represent whole-core sections (lavas plus interstitial materials), analysed by Chauvel et al. (2009). Site 801 MORB and TAB (Top Alkali Basalt) data were from pure basalt cores using εHf and εNd data for the data points (Pearce et al., 1999) with additional data on εNd only (Hauff et al., 2003) used to establish their dispersion. Fig. 7b-c include further sediment data from Plank et al. (2007) and Vervoort et al. (2011). Mixing lines between M (residual FAB mantle) and S_1 (subduction component 1) and between H (hybrid mantle wedge) and S_2 (subduction component 2) constrain the compositions of bulk subducted materials.

Figure 8. Plots of εHf, εNd, and $^{87}Sr/^{86}Sr$ and $^{207}Pb/^{204}Pb$ isotope ratios against Δ8/4, where Δ8/4 is the displacement from the Northern Hemisphere Reference Line

921 (NHRL) in $^{208}Pb/^{204}Pb$-$^{206}Pb/^{204}Pb$ space. By definition, points on the NHRL have
922 Δ8/4 values of 0, while the Indian-Pacific mantle domain boundary on the same
923 diagram has a value of +20. Philippine Sea and Western Pacific mantle domains (Fig.
924 5a) are drawn as rectangles either side of this value. Alteration will, however, displace
925 these domains to lower Δ8/4. The two subduction trends (modeled as described in the
926 text) are clearly defined as running between 1) a residual FAB, 'Indian' domain,
927 mantle (M) and a 'Pacific' domain slab melt (S_1), and 2) a hybrid (slab melt +
928 depleted mantle) mantle wedge (H) and a combination of Pacific Pelagic Sediment
929 (PPS) and Pacific Altered Oceanic Crust (AOC) fluid or melt (S_2). εHf and εNd
930 values of S_1 and S_2 are constrained by Fig. 5 and used in turn to constrain the Pb and
931 Sr end-member compositions.

932

933 Figure 9. A conceptual model linking the isotope interpretations to the geodynamics
934 of subduction initiation. A. The model starts at a hypothetical transform fault at the
935 Izanagi (IZA)-Pacific (PAC) plate boundary. B) Shallow, slow subduction then
936 accretes sediment, allowing a sediment-free plate to subduct. C) Once subduction is
937 sufficiently deep for phase transformation of subducted crust to eclogite facies, initial
938 rapid rollback leads to extension with formation of FAB with no or little subduction
939 input. D) As the slab sinks further, it heats up to melting temperatures while still at
940 shallow depth, and these slab melts then interact with residual mantle to produce low-
941 Si boninites. E) Further roll-back and perhaps the start of dip-slip subduction causes
942 accreted sediment to subduct and contribute to off-axis magma genesis, with fluid
943 interacting with unmelted mixtures of residual mantle and slab melt (hybrid mantle
944 wedge) to produce high-Si boninites. Alternative, but we believe less likely,
945 mechanisms for explaining the isotopic features are discussed in the text. Note that

946 the model covers only the c. 52-50Ma period immediately following subduction
947 initiation and so does not extend to the subsequent (c. 50-44Ma) growth and initial
948 rifting of the protoarc and transition into normal arc magmatism. Similarly, the model
949 does not extend to include the c. 50-49 Ma extensional event that formed the forearc
950 basalts at IODP Site U1438 further to the west (Yogodzinski et al, 2018; see also Fig.
951 1 and Fig. 5 of this paper) and which significantly post-dates the forearc basalt
952 spreading event depicted in Fig. 9C (Reagan et al., 2019). IMM and PMM =
953 Indian/Pacific MORB Mantle.

954

Figure 1

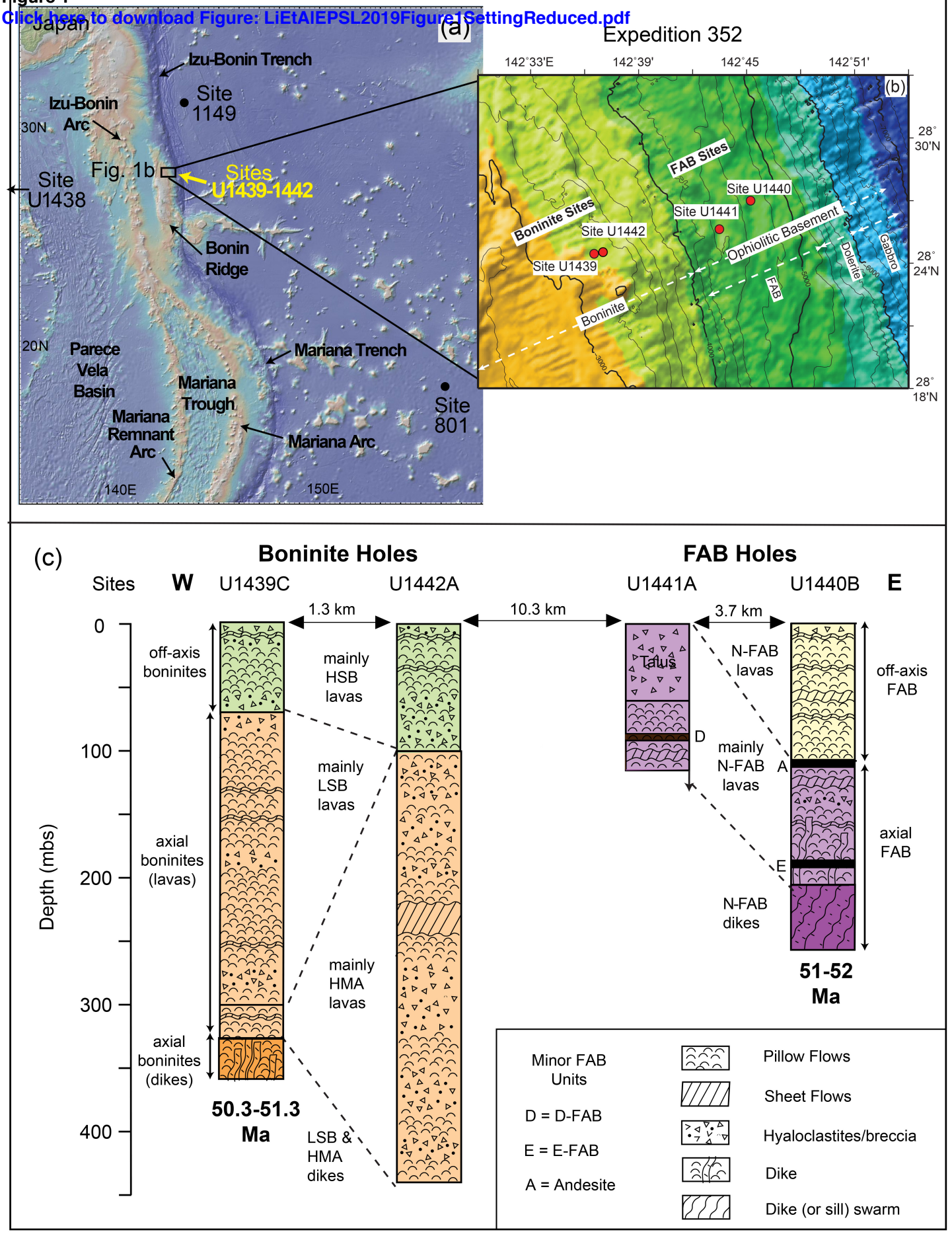

Figure 2

Click here to download Figure: LietalEPSL2019Figure2IsotopeStrat.pdf

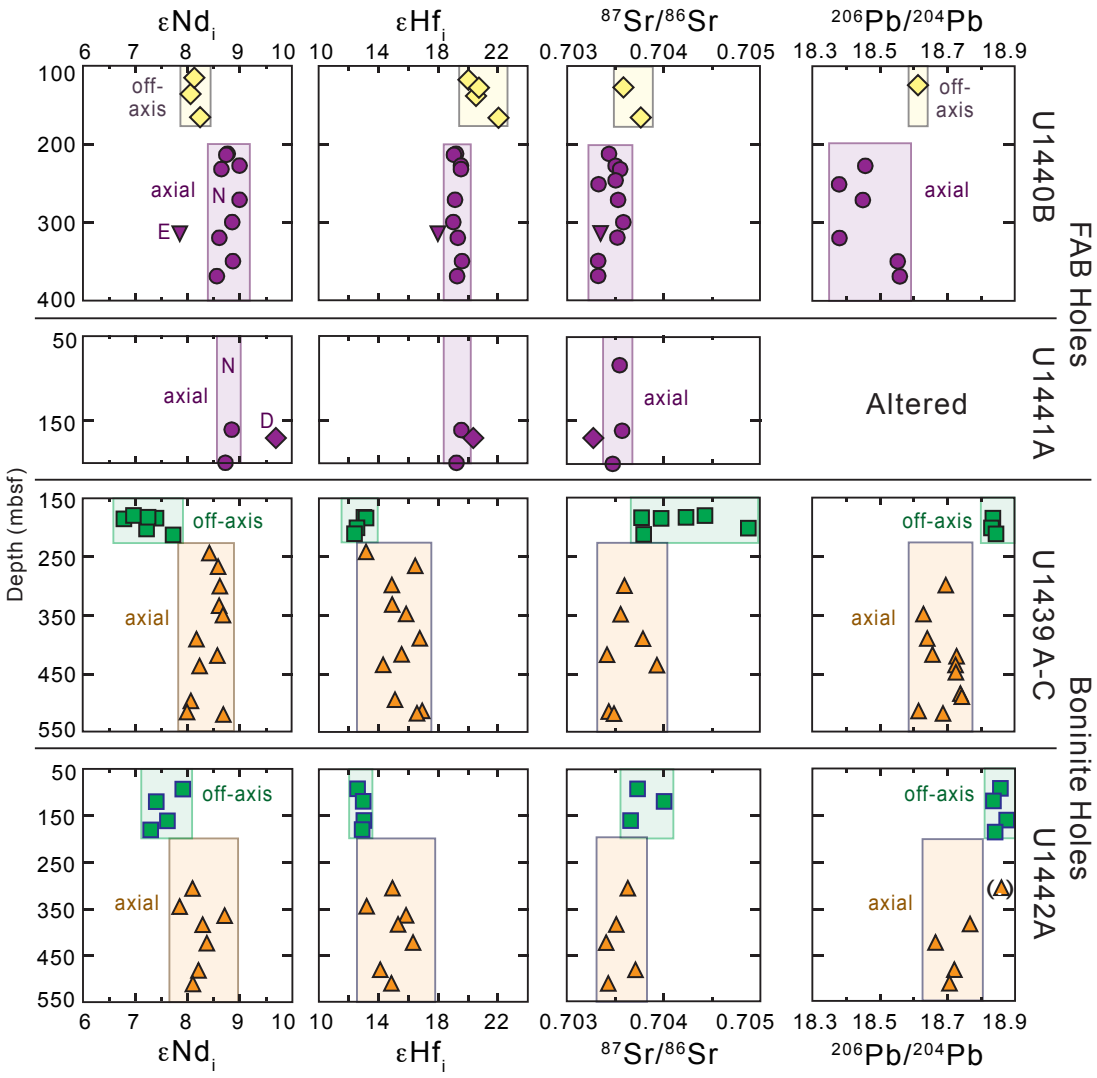

Figure 3

Click here to download Figure: LietalEPSL2019Figure3ExtendedREE.pdf

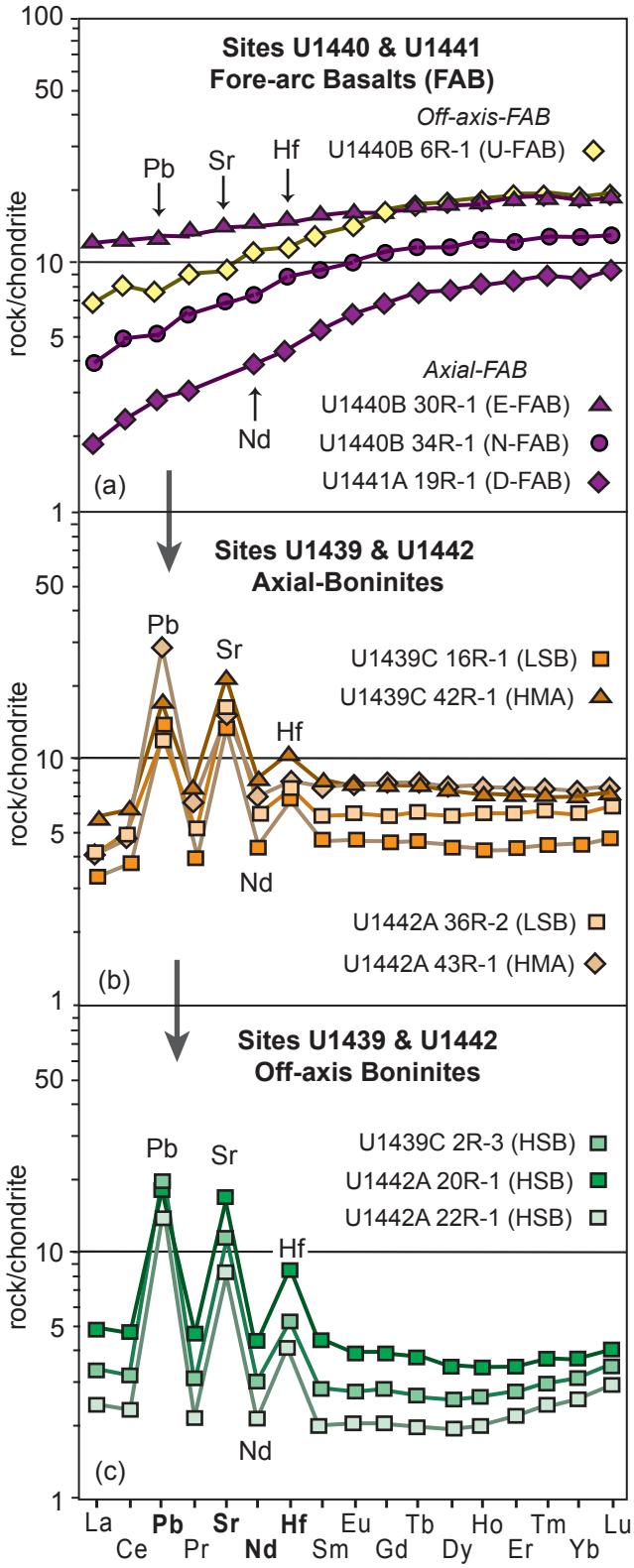

Figure 4

Click here to download Figure: LietalEPSL2019Figure4NdHfSrPbIsotopes.pdf

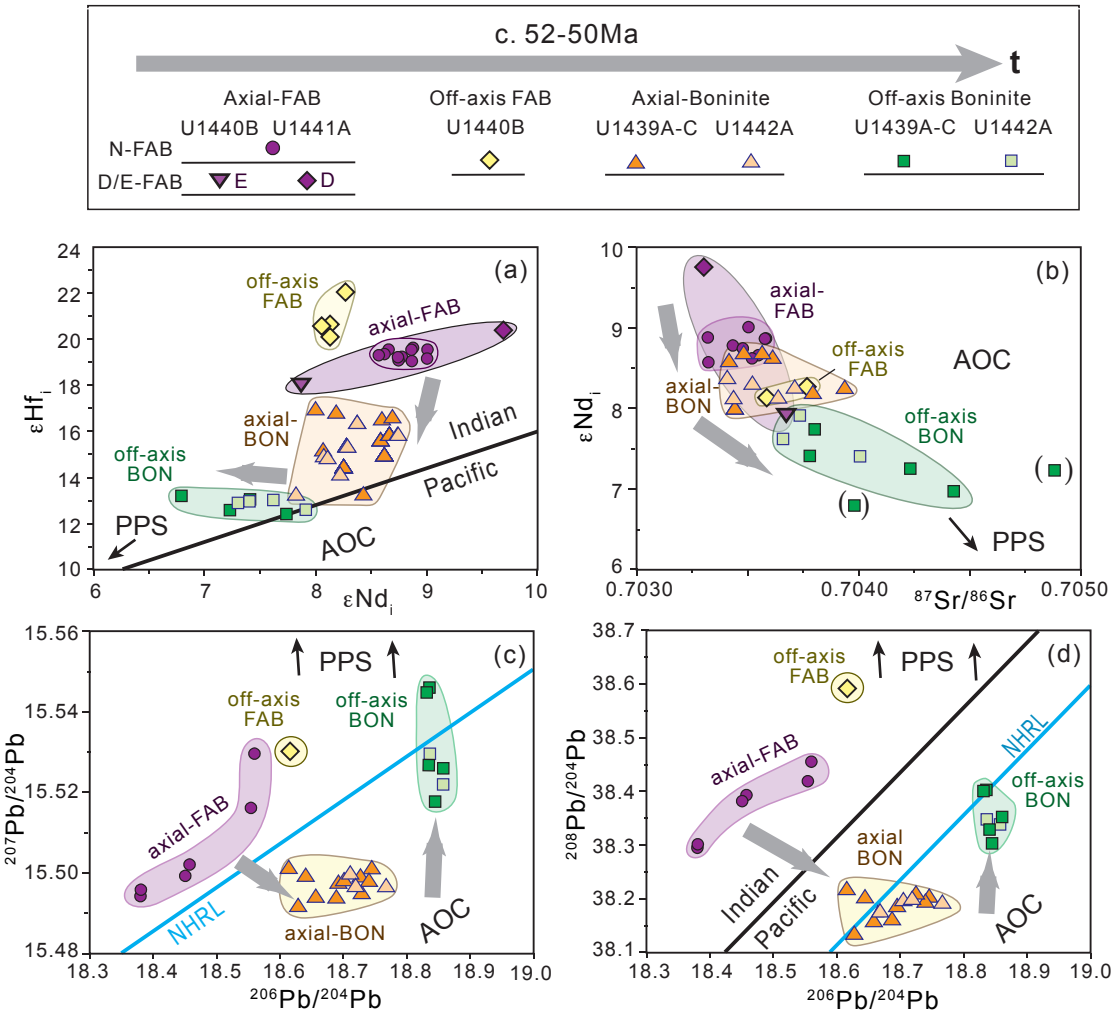

Figure 5

Click here to download Figure: LiEtAlEPSL2019Figure5HfNd.pdf

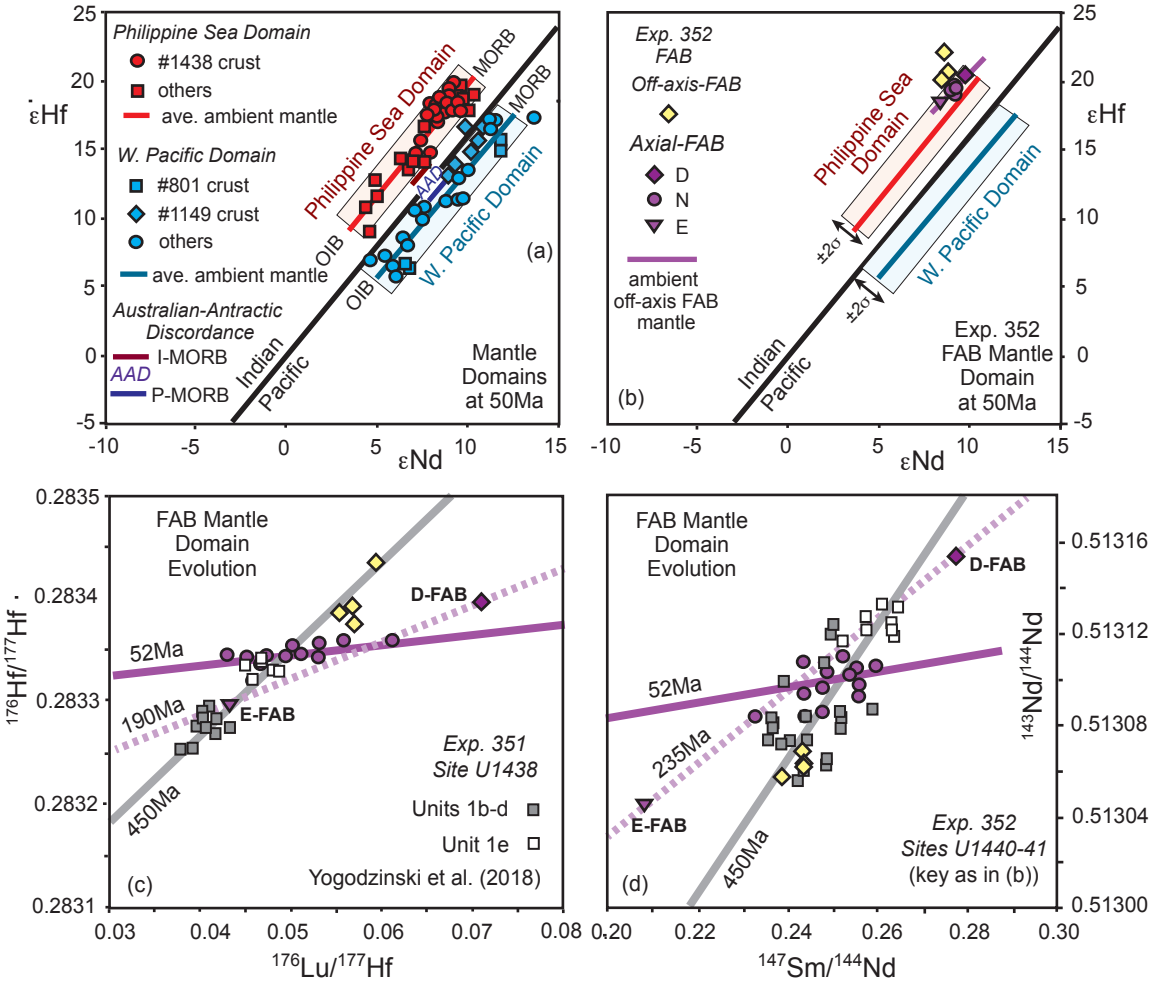

Figure 6

Click here to download Figure: LiEtAlEPSL2019Figure6HfNdIsotopeRatioPlots.pdf

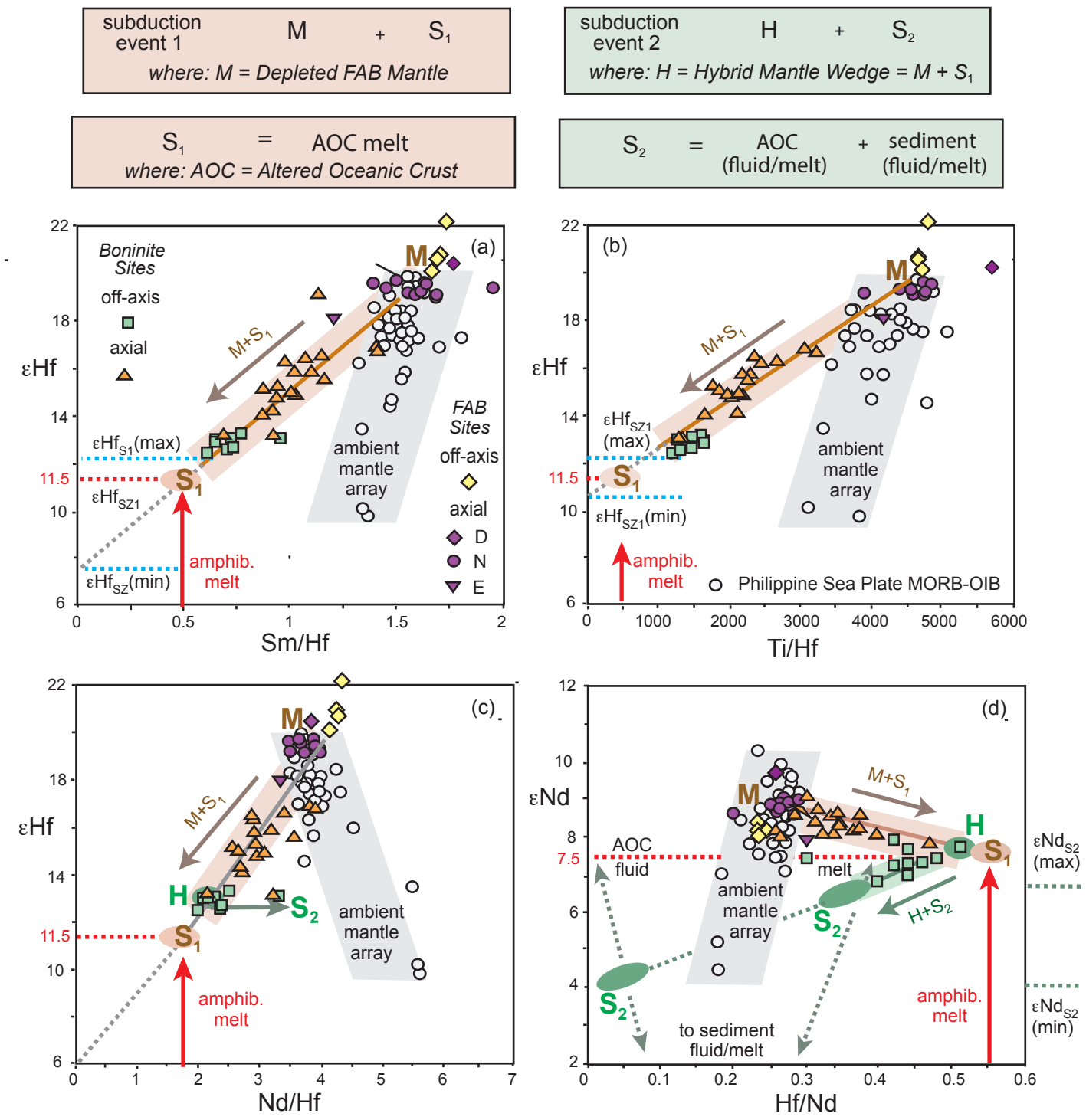

Figure 7

Click here to download Figure: LiEtAlEPSL2019Figure7HfNdSubductionComponents.pdf

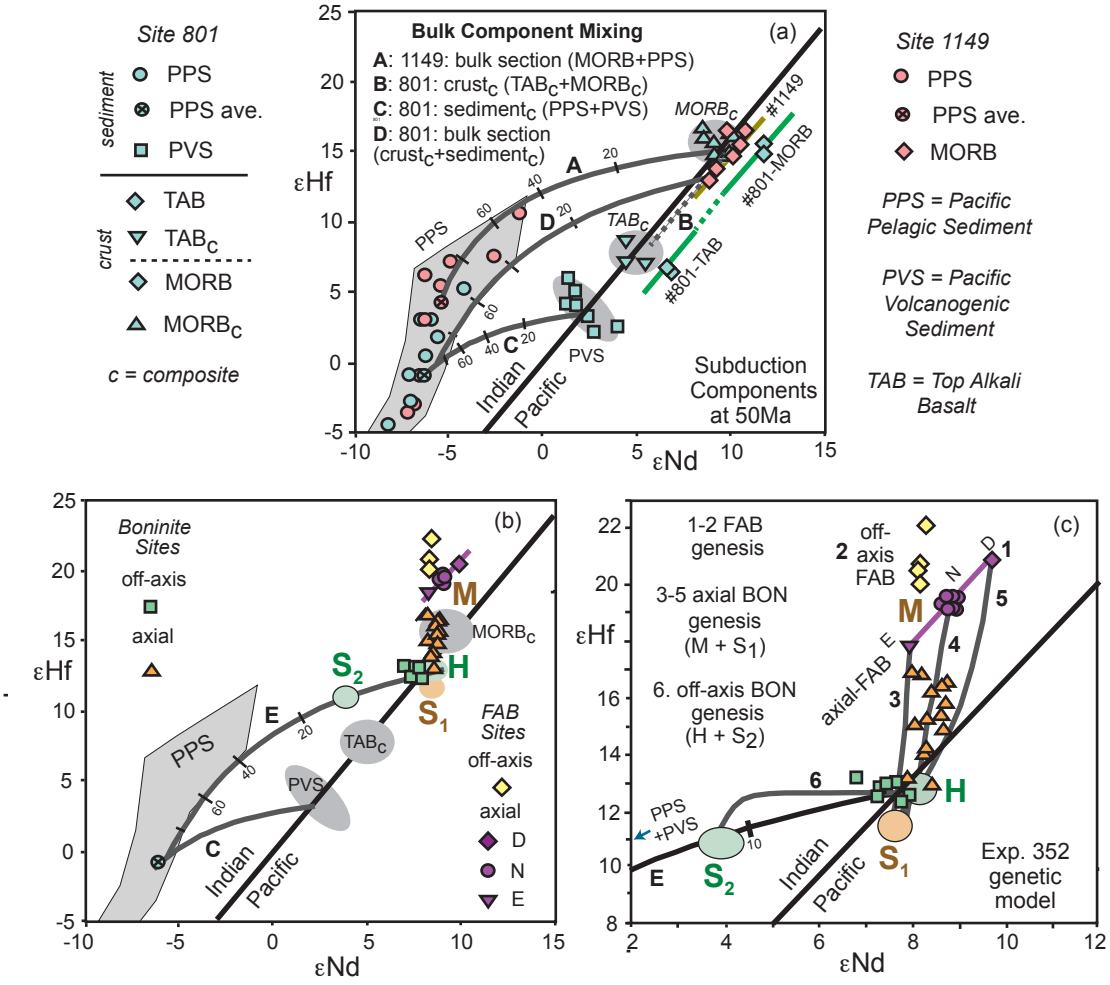

Figure 8

Click here to download Figure: LiEtAlEPSL2019Figure8DeltaPb.pdf

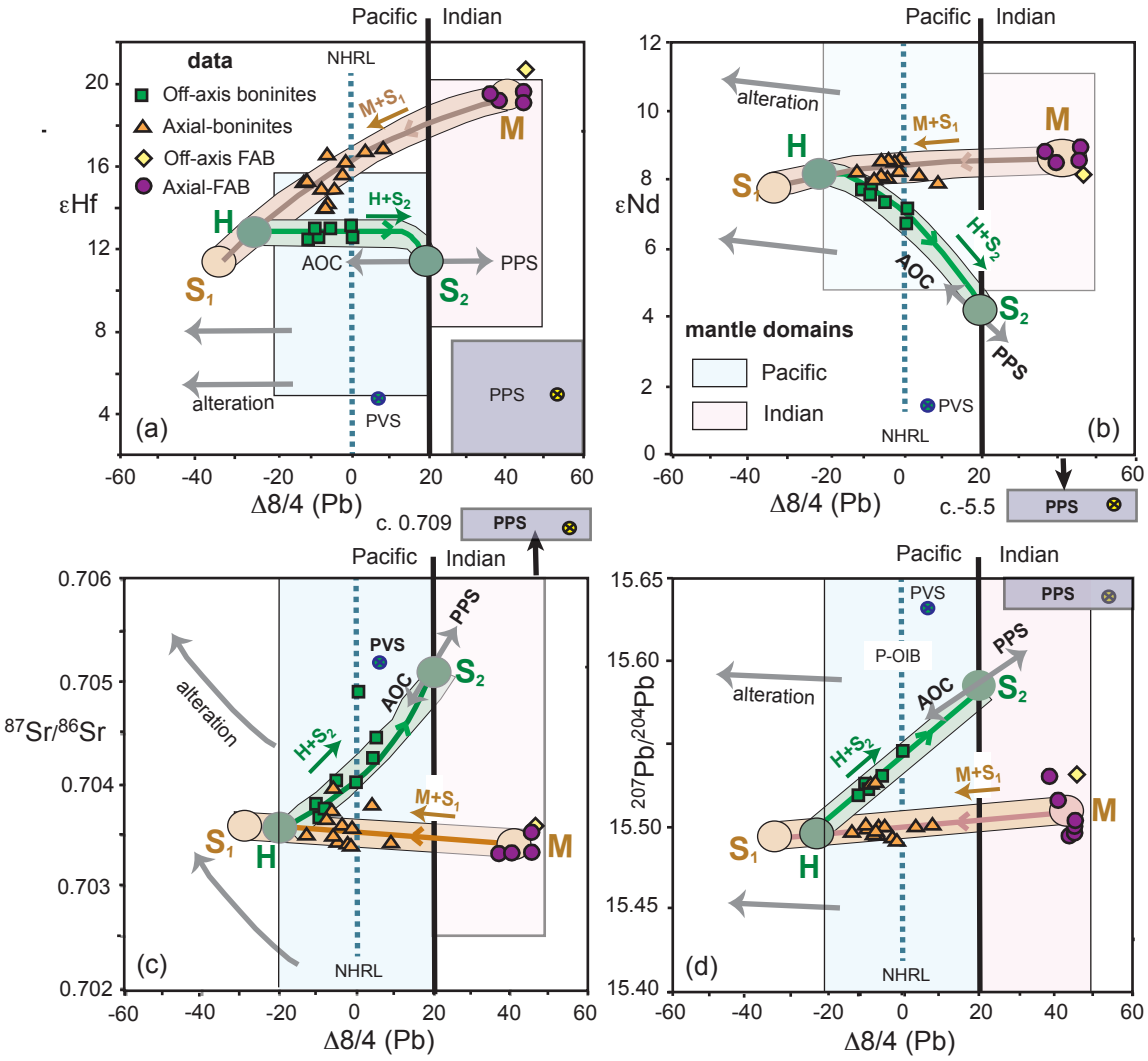

Figure 9

Click here to download Figure: LiEtAlEPSL2019Figure9IsotopeEvolution.pdf

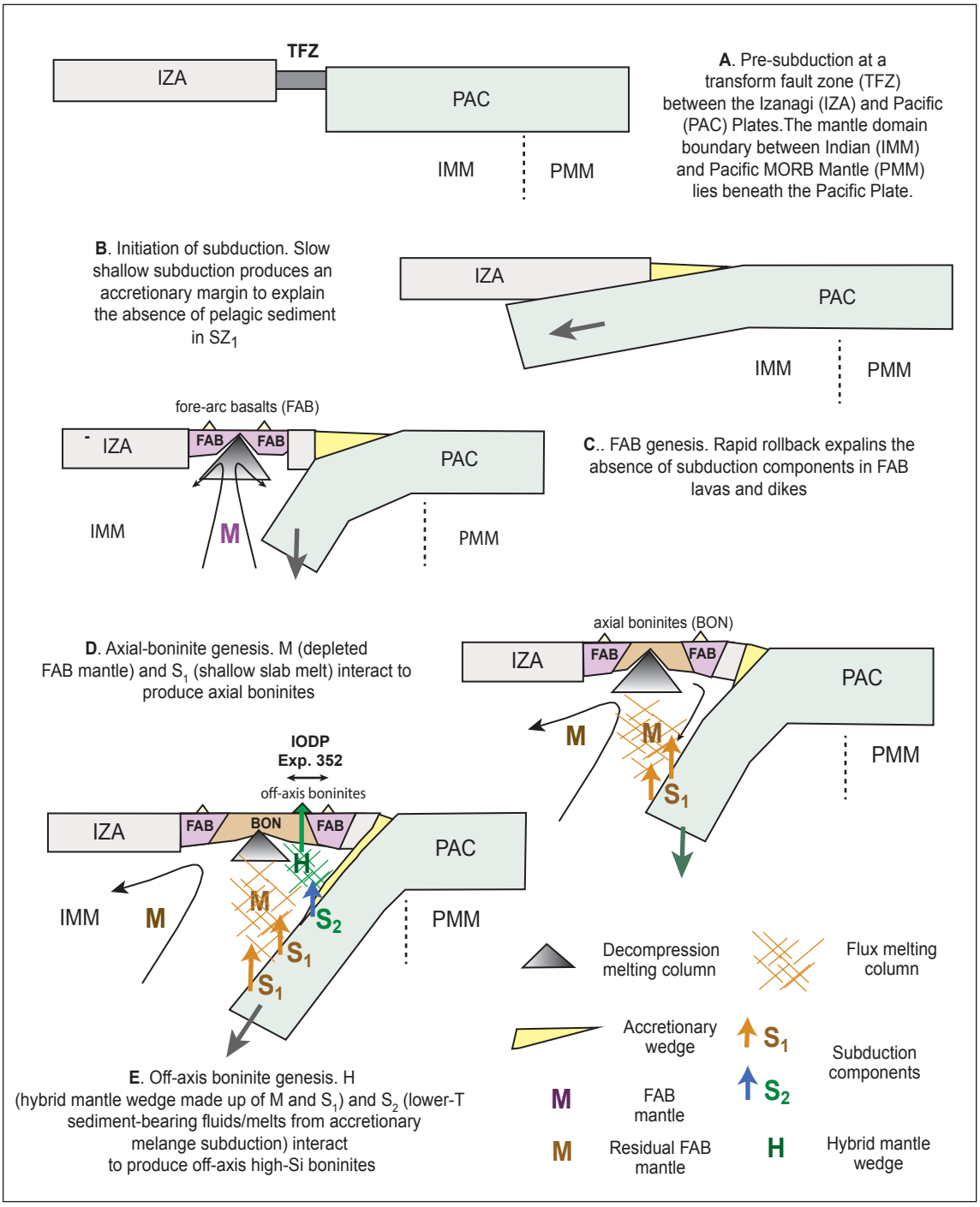

Table 1

Click here to download Table: LietalEPSL2019Table1.docx

Sample	Series	Type	Unit	Depth	$^{206}Pb/^{204}Pb$	$^{207}Pb/^{204}Pb$	$^{208}Pb/^{204}Pb$	$^{87}Sr/^{86}Sr$	εNd_{50}	εHf_{50}
U1440B										
6R-1	Off-axis	N-FAB	2	127.11	18.6154	15.5301	38.592	0.703581	8.1	20.7
12R-2	Off-axis	N-FAB	3	165.14		altered		0.703768	8.3	22.1
19R-1*	Axial	N-FAB	6	227.40	18.4577	15.5021	38.393	0.703482	9.0	19.6
24R-1*	Axial	N-FAB	7	251.20	18.3803	15.4942	38.295	0.703327		
26R-1*	Axial	N-FAB	8	271.14	18.4508	15.4992	38.382	0.703470	9.0	19.2
29R-1	Axial	N-FAB	11	299.75		altered		0.703584	8.9	19.1
30R-1	Axial	E-FAB	13	309.53		altered		0.703426	8.1	17.8
31R-1*	Axial	N-FAB	14	319.74	18.3809	15.4958	38.302	0.703521	8.6	19.4
34R-1	Axial [D]	N-FAB	15	349.72	18.5544	15.5161	38.419	0.703322	8.9	19.6
36R-1	Axial[D]	N-FAB	15	368.94	18.5600	15.5296	38.455	0.703324	8.6	19.3
U1441A										
18R-1	Axial	N-FAB	2	160.97		altered		0.703578	8.9	19.5
19R-1	Axial	D-FAB	3	171.16		altered		0.703305	9.7	20.4
22R-1	Axial	N-FAB	4	199.85		altered		0.703479	8.7	19.2
U1439C										
2R-3	Off-axis	HSB	2a	185.13	18.8358	15.5460	38.403	0.703981	6.8	13.2
4R-1	Off-Axis	HSB	3a	201.86	18.8341	15.5438	38.404	0.704884	7.2	12.6
16R-1	Axial	LSB	6	299.76	18.6961	15.4979	38.189	0.703604	8.6	14.9
22R-1	Axial	LSB	6	349.19	18.6305	15.4918	38.135	0.703565	8.7	15.9
26R-3	Axial	LSB	7	390.66	18.6420	15.4993	38.204	0.703794	8.2	16.8
29R-2	Axial	LSB	8	418.27	18.6566	15.4938	38.158	0.703423	8.6	15.6
41R-1	Axial[D]	LSB	10	515.09	18.6154	15.5012	38.219	0.703443	8.0	17.0
42R-1	Axial[D]	HMA	10	518.88	18.6883	15.4943	38.161	0.703495	8.7	16.6
U1442A										
11R-1	Off-axis	HSB	1a	92.22	18.8572	15.5219	38.339	0.703736	7.9	12.6
15R-1	Off-axis	HSB	1b	119.40	18.8364	15.5295	38.348	0.704007	7.4	13.0
20R-1	Off-axis	HSB	1c	160.64	18.8751	15.5245	38.356	0.703661	7.6	13.0
35R-1	Axial	LSB	2b	306.01	18.8603	15.5259	38.350	0.703634	8.1	14.9
43R-1	Axial	HMA	2b	383.86	18.7666	15.4966	38.190	0.703515	8.3	15.3
47R-1	Axial	HMA	3	423.10	18.6646	15.4914	38.177	0.703409	8.4	16.3
53R-1	Axial	HMA	4	481.39	18.7205	15.4967	38.197	0.703714	8.2	14.1
56R-1	Axial	LSB	4	510.49	18.7054	15.4993	38.198	0.703433	8.1	14.9

- glass separates used for Pb and Sr isotope analyses (except 31R-1: Pb only)